A seasonal algorithm of the snow-covered area fraction for mountainous terrain

Nora Helbig [1], Michael Schirmer [1], Jan Magnusson [2], Flavia Mäder [1,3], Alec van Herwijnen [1], Louis Quéno [1], Yves Bühler [1], Jeff S. Deems [4], and Simon Gascoin [5]

[1]WSL Institute for Snow and Avalanche Research SLF, Davos, Switzerland
[2]Statkraft AS, Oslo, Norway
[3]Institute of Geography, University of Bern, Bern, Switzerland
[4]National Snow and Ice Data Center, University of Colorado, Boulder, CO, USA
[5]Centre d'Etudes Spatiales de la Biosphère, CESBIO, Univ. Toulouse, CNES/CNRS/INRAE/IRD/UPS, 31401 Toulouse, France

Correspondence: Nora Helbig (norahelbig@gmail.com)

Abstract. The snow cover spatial variability in mountainous terrain changes considerably over the course of a snow season. In this context, fractional snow-covered area ($fSCA$) is ~~therefore~~ an essential model parameter characterizing how much ~~of the~~ ground surface in a grid cell is currently covered by snow. We present a seasonal $fSCA$ algorithm using a recent scale-independent $fSCA$ parameterization. For the seasonal implementation, we track snow depth (HS) and snow water equivalent (SWE), and account for several alternating accumulation-ablation phases. Besides tracking HS and SWE, the seasonal $fSCA$ algorithm only requires ~~computing~~ subgrid terrain parameters from a fine-scale summer digital elevation model. We implemented the new algorithm in a multilayer energy balance snow cover model. ~~For a spatiotemporal evaluation of~~ To evaluate the spatiotemporal changes in modelled $fSCA$, we compiled three independent $fSCA$ data sets ~~. Evaluating modelled 1 km $fSCA$ seasonally with $fSCA$~~ derived from airborne-acquired fine-scale HS data, ~~satellite-~~ as well as ~~terrestrial camera-derived~~ $fSCA$ ~~showed overall~~ data derived from satellite and terrestrial imagery. Overall, modelled daily 1km-$fSCA$ values had normalized root mean square errors of respectively ~~9 %, 20 % and 22~~ 7 %, 12 % and 21 %, and ~~represented seasonal trends well. The overall good model performance suggests that the~~ some seasonal trends were identified. Comparing our algorithm performances to the performances of the CLM5.0 $fSCA$ algorithm implemented in the multilayer snow cover model demonstrated that our full seasonal $fSCA$ algorithm better represented seasonal trends. Overall, the results suggest that our seasonal $fSCA$ algorithm can be applied in other geographic regions by any snow model application.

1 Introduction

In mountainous terrain, the large spatial variability of the snow cover is driven by the interaction of meteorological variables with the underlying topography. Over the course of a winter season, the dominating topographic interactions with wind, precipitation and radiation vary considerably, ~~which generate the~~ generating characteristic seasonal dynamics of spatial snow depth variability (e.g. Luce et al., 1999). This spatial variability, or how much of the ground is actually covered by snow, is typically characterized by the fractional snow-covered area ($fSCA$). $fSCA$ is a crucial parameter in model applications such as weather forecasts (e.g. Douville et al., 1995; Doms et al., 2011), hydrological modelling (e.g. Luce et al., 1999; Thirel et al., 2013; Magnusson et al., 2014; Griessinger et al., 2016, 2019) or avalanche forecasting (Bellaire and Jamieson, 2013; Horton and Jamieson, 2016; Vionnet et al., 2014), and is also used for climate scenarios (e.g. Roesch et al., 2001; Mudryk et al., 2020).

$fSCA$ can be retrieved from various satellite sensor imagessuch as from , including Moderate Resolution Imaging Spectroradiometer (MODIS) or Sentinel-2 (e.g. Hall et al., 1995; Painter et al., 2009; Drusch et al., 2012; Masson et al., 2018; Gascoin et al., 2019). However, a Nevertheless, solutions are required to correct for temporal and spatial inconsistent coverage due to time gaps between satellite revisits, data delivery and the frequent presence of clouds requires additional solutions (Parajka and Blöschl, 2006; Gascoin et al., 2015). Though fine-scale spatial snow cover models provide spatial snow depth distributions which that could be used to derive coarse-scale $fSCA$, applying such models to larger regions is generally not feasiblewhich . This is in part due to computational cost, a lack of detailed input data and limitations in model structure or parameters. While some of these limitations can be overcome using current snow cover model advances applying data assimilation routines (e.g. Andreadis and Lettenmaier, 2006; Nagler et al., 2008; Thirel et al., 2013; Griessinger et al., 2016; Huang et al., 2017; Baba et al., 20 (e.g. Andreadis and Lettenmaier, 2006; Nagler et al., 2008; Thirel et al., 2013; Griessinger et al., 2016; Huang et al., 2017; Baba et al., 20 , the inherent uncertainties in input or assimilation data still remain. Computationally efficient subgrid $fSCA$ parameterizations, accounting for unresolved snow depth variability, are therefore currently still the method of choice for coarse-scale model systems, such as weather forecast, land surface and earth system models. Furthermore, $fSCA$ parameterizations are essential when assimilating satellite snow-covered area data in model systems (e.g. Zaitchik and Rodell, 2009)

Several compact, closed-form $fSCA$ parameterizations were suggested for coarse-scale model applications (e.g. Douville et al., 1995; Roesch et al., 2001; Yang et al., 1997; Niu and Yang, 2007; Su et al., 2008; Zaitchik and Rodell, 2009; Swenson and Lawrence, 2012). Most of these $fSCA$ parameterizations were heuristically developed. Some parameterizations introduced subgrid terrain parameters (e.g. Douville et al., 1995; Roesch et al., 2001; Swenson and Lawrence, 2012). The $tanh$-form, suggested by Yang et al. (1997), was later confirmed by integrating theoretical log-normal snow distributions and fitting the resulting parametric depletion curves using the spatial snow depth distribution (σ_{HS}) in the denominator of fitted $fSCA$ curves (Essery and Pomeroy, 2004). Through advances in remote sensing techniques, fine-scale spatial snow depth (HS) data became more readily available allowing to empirically parameterize σ_{HS} in complex topography at peak of winter (PoW) or during accumulation (Helbig et al., 2015b; Skaugen and Melvold, 2019). By parameterizing σ_{HS} using subgrid terrain parameters, Helbig et al. (2015b) enhanced expanded the $tanh$-$fSCA$ parameterization of Essery and Pomeroy (2004) by accounting to account for topographic influence. FurthermoreRecently, Helbig et al. (2021) re-evaluated this empirically derived $fSCA$ parameterization with high-resolution spatially distributed snow depth data spatial HS sets from 7 different geographic regions at PoW. They introduced a scale-dependency in the dominant scaling variables that improved the empirical $fSCA$ parameterization by making , and made it applicable across spatial scales $\geq$ 200 m by introducing a scale-dependency in the dominant model descriptors.

Many studies highlighted that the same mean HS in early winter or in late spring can lead to substantially different $fSCA$ (Luce et al., 1999; Niu and Yang, 2007; Magand et al., 2014), a phenomenon that . This has led to the introduction of hysteresis in some $fSCA$ parameterizations (e.g. Luce et al., 1999)(e.g. Luce et al., 1999; Swenson and Lawrence, 2012). Previously found interannual time-persistent correlations between topographic parameters and snow depth distributions (e.g. Schirmer et al., 2011; Schirmer and Lehning, 2011; Revuelto et al., 2014; López-Moreno et al., 2017) suggest indeed that a time-dependent $fSCA$ implementation might be feasible. However, a seasonal model implementation of a closed form $fSCA$ parameterization also needs to account for alternating snow accumulation and melt events during the season. Especially at lower elevations and increasingly so with climate change, the separation of the depletion curve in only one accumulation period followed by a melting period is no longer applicable (e.g. Egli and Jonas, 2009). A seasonal $fSCA$ implementation in mountainous regions that accounts for these alternating periods is challenging. While some seasonal $fSCA$ implementations of varying complexities were previously proposed (e.g. Niu and Yang, 2007; Su et al., 2008; Egli and Jonas, 2009; Swenson and Lawrence, 2012; Nitta et al., 2014; Magnusson et al., 2014; Riboust et al., 2019) a detailed evaluation of seasonally parameterized $fSCA$ with $fSCA$ derived from high-resolution spatial ~~as well as~~ and temporal HS data or snow products is currently still missing.

~~This article presents~~ Here, we present a seasonal $fSCA$ implementation and ~~its temporal evaluation~~ evaluate it with high-resolution observation data in various geographic regions throughout Switzerland. The algorithm is based on the $fSCA$ parameterization for complex topography proposed by Helbig et al. (2015b, 2021)~~and applies~~. We apply two different empirical parameterizations for the spatial snow depth distribution, ~~namely the ones~~ from Egli and Jonas (2009) and Helbig et al. (2021)~~. The seasonal $fSCA$ algorithm allows for alternating snow~~ , with seasonal and current HS values to describe the hysteresis. Snow accumulation and melt events during the season ~~by accounting for~~ are accounted for by tracking the history of ~~previous~~ HS and SWE values ~~.~~ throughout the snow season. We implemented the algorithm in a multilayer energy balance snow cover model (modified JIM, the JULES investigation model by Essery et al. (2013)) which we ran with COSMO-1 (operated by MeteoSwiss) reanalysis data, measured HS and RhiresD precipitation data (MeteoSwiss). The seasonal performance of this algorithm was evaluated using ~~daily modelled 1 km $fSCA$ in Switzerland. For the evaluation we compiled~~ $fSCA$ data sets from terrestrial cameras, airborne surveys and satellite imagery. ~~With this we were able to evaluate~~ This allowed us to assess modelled $fSCA$ using independent HS data sets ~~in~~ with high spatial resolution and snow products ~~in~~ with high temporal resolution. We further implemented the Community Land Model (CLM5.0) $fSCA$ algorithm accounting for hysteresis in accumulation and ablation (Lawrence et al., 2018), which is based on the work of Swenson and Lawrence (2012), in the multilayer energy balance snow cover model. Modelled $fSCA$ from the CLM5.0 $fSCA$ algorithm was also assessed with the measured $fSCA$ data sets and the performances compared to those of our seasonal $fSCA$ algorithm.

2 Fractional snow-covered area algorithm

~~The~~ In the following, we introduce the seasonal $fSCA$ algorithm ~~consists of four parts (cf. upper large box in Figure 1). The first part describes the closed form~~ in two parts. First we present the closed-form $fSCA$ parameterization ~~using snow depth HS and standard deviation of subgrid snow depth~~ derived by Helbig et al. (2015b). This formulation uses the spatial subgrid variability of snow depth (σ_{HS}) and snow depth HS of a grid cell. ~~The second and third part describe two different σ_{HS} parameterizations, one derived for mountainous terrain developed on PoW data ($\sigma_{HS}^{\text{topo}}$) and one for flat terrain developed~~

~~on accumulation data ($\sigma_{HS}^{\text{flat}}$). These are the inputs to the~~ To derive σ_{HS}, we used two different statistical parameterizations. Second, we describe our seasonal $fSCA$ ~~function in part one.The fourth part handles~~ algorithm, i.e. how we handle the distinctly different paths between σ_{HS} and HS during accumulation and ~~ablation periods, the hysteresis. This last part thus describes the technical aspects for a seasonal implementation of $fSCA$, presented in part one, which requires tracking HS and SWE over the season, deriving extreme values of HS and SWE as well as the two σ_{HS} parameterizations presented in part two and three~~melt periods, i.e. the hysteresis.

2.1 $fSCA$ parameterization

~~We use the $fSCA$~~ The core of our seasonal algorithm is the PoW parameterization of Helbig et al. (2015b) ~~derived by integrating a theoretical normal snow depth distribution at PoW, assuming spatially homogeneous melt and by fitting the resulting depletion curves over a range of coefficients of variation CV (standard deviation divided by its mean) in snow depth ranging from 0.06 to 1.00:~~ relating $fSCA$ to HS and σ_{HS}:

$$fSCA = \tanh(1.3\,\frac{HS}{\sigma_{HS}})\,. \tag{1}$$

~~Using~~ By including both HS and σ_{HS}~~in Eq. (1) allowed Helbig et al. (2015b) to introduce~~, this formulation accounts for the close link between spatial subgrid snow depth variability and topography in $fSCA$.

Although Eq. (1) ~~uses current HS in the numerator and σ_{HS} at seasonal maximum HS in the denominator, which we adapt here for a seasonal $fSCA$ algorithm as described in Section ??. For the~~ was derived for PoW, in our seasonal $fSCA$ algorithm we ~~further compute~~ apply it throughout the entire snow season by using two different parameterizations for σ_{HS}~~differently over flat and steep terrain ($\sigma_{HS}^{\text{flat}}$, $\sigma_{HS}^{\text{topo}}$) which is described in the following.~~, one accounting for subgrid topography (Helbig et al., 2021), while the second only depends on HS (Egli and Jonas, 2009).

2.2 ~~σ_{HS} parameterization for mountainous terrain at peak of winter ($\sigma_{HS}^{\text{topo}}$)~~

~~Helbig et al. (2021) could use the same functional form to empirically describe~~

σ_{HS} parameterization accounting for topography

We use the PoW subgrid parameterization for σ_{HS} in mountainous terrain originally developed by Helbig et al. (2015b) and later extended by Helbig et al. (2021). This parameterization accounts for the impact of topography on the spatial snow depth ~~variability σ_{HS} at PoWin mountainous terrain than Helbig et al. (2015b) when using snow data sets from seven different geographic regions and two continents:~~ distribution at PoW:

$$\sigma_{HS}^{\text{topo}\,\text{Helbig}} = HS^c\,\mu^d\,\exp[-(\xi/L)^2]\,. \tag{2}$$

~~albeit that they introduced~~

The parameterization contains two scale-dependent parameters ~~$e(L)$ and $d(L)$ in Eq. (2), which enhanced the~~ c and d:

$$c = 0.5330\, L^{0.0389}$$
$$d = 0.3193\, L^{0.1034}\,. \tag{3}$$

This σ_{HS} ~~parameterization across spatial scales~~ subgrid parameterization is generally valid for domain sizes (i.e. the coarse grid cell size) $L \geq$200 m. ~~$\sigma_{HS}^{\mathrm{topo}}$ (~~Besides domain size L, Eq. (~~2)) was parameterized using spatial mean snow depth~~ 3) requires snow depth HS and subgrid summer terrain parameters ~~: a~~ μ and ξ. The mean squared slope related parameter ~~μ and a terrain correlation length ξ for each domain size~~ $\mu = \left\{\overline{[(\partial_x z)^2 + (\partial_y z)^2]}/2\right\}^{1/2}$ is derived using partial derivatives of subgrid terrain elevations z, i.e. from a summer digital elevation model (DEM). The correlation length $\xi = \sqrt{2}\sigma_z/\mu$ is derived for each L ~~(coarse grid cell). Given that the σ_{HS} parameterization~~ using the standard deviation σ_z of terrain elevations z. The L/ξ-ratio in Eq. (~~2)accounts for the impact of topography on σ_{HS}, we indicate that with 'topo' ($\sigma_{HS}^{\mathrm{topo}}$). For more~~ 3), describes the frequency of topographic features of length scale ξ in a domain L. All terrain parameters are derived on linearly detrended summer DEMs (Helbig et al., 2015b). More details on Eq. (2) ~~we refer to Helbig et al. (2015b, 2021) to keep the focus of this study on the seasonal $fSCA$ algorithm and its evaluation.~~ and (3) can be found in Helbig et al. (2015b, 2021).

2.2 ~~σ_{HS} parameterization for flat terrain during accumulation ($\sigma_{HS}^{\mathrm{flat}}$)~~

~~$\sigma_{HS}^{\mathrm{topo}}$ was developed for grid cells in mountainous terrain. Here, we present a σ_{HS} that can be applied in flat terrain, which we indicate with 'flat' ($\sigma_{HS}^{\mathrm{flat}}$). Egli and Jonas (2009) derived an empirical parameterization for~~

σ_{HS} parameterization not accounting for topography

The second σ_{HS} ~~during accumulation by fitting mean~~ parameterization was developed by Egli and Jonas (2009) by fitting daily spatial HS means and standard deviation of ~~77 flat field~~ HS ~~measurements distributed throughout Switzerland~~ from 77 weather stations distributed throughout the Swiss Alps over six consecutive winter seasons during accumulation season. The resulting parameterization ~~solely~~ uses HS and a constant fit parameter:

$$\sigma_{HS}^{\mathrm{flat}\,\mathrm{Egli}} = HS^{0.839}\,. \tag{4}$$

~~Sketch of the seasonal $fSCA$ algorithm as used for one grid cell.~~ This parameterization does not account for the impact of topography on σ_{HS}.

2.2 ~~Seasonal $fSCA$ implementation~~

~~For the implementation of our seasonal~~

2.2 Seasonal $fSCA$ algorithm

To use the above $fSCA$ ~~algorithm (cf.~~ formulation (Eq. 1~~-3) in any snow cover model, tracking snow information (i.e. keeping the history) through several alternating accumulation-ablation phases is required. By tracking snow information we can use~~

current to extreme HS values to derive σ_{HS} (Eq. (2) and (3))and) throughout an entire snow season, we track changes in HS with time. This is done to account for the fact that after a snowfall, $fSCA$ (Eqcan dramatically increase. Once the new snow has settled or started to melt, $fSCA$ values then generally return to similar values as before. We account for this by computing two $fSCA$ values in parallel, namely a seasonal $fSCA$ ($fSCA_{\text{season}}$) and a new snow $fSCA$ ($fSCA_{\text{nsnow}}$). $fSCA_{\text{season}}$ accounts for the entire history of the snow season up to the current time step, and thus all processes shaping the spatial snow depth distribution. It is therefore computed using $\sigma_{HS}^{\text{Helbig}}$ (1))Eq. We search extreme points in time 3), which accounts for subgrid topography. $fSCA_{\text{nsnow}}$ only accounts for contributions by recent snowfall. As a snowfall generally covers most of the topography within a grid cell (i.e. all surfaces are initially covered by snow), we use $\sigma_{HS}^{\text{Egli}}$ (Eq. 4), which does not account for subgrid topography.

$fSCA_{\text{season}}$

To compute $fSCA_{\text{season}}$, we use extreme HS values at each time step per grid cell (Figure 1a). It is important to note that we identify these extremes using SWE to avoid influences of snow settling. Since rather than HS, as due to snow settlement HS values can peak even before a precipitation event has ended. However, as our $fSCA$ algorithm needs requires HS as input, we search for extreme SWE values in time, and use the corresponding HS valuesof SWE extreme points are applied. . In the following we will not specify this anymorebut instead , and only refer to extreme values of HS(minimum, maximum) or HS differences. A full seasonal . To compute $fSCA_{\text{season}}$ we use $\sigma_{HS}^{\text{Helbig}}$ (Eq. 3) in the $fSCA$ algorithmformulation (Eq. 1) as follows:

$$fSCA_{\text{season}} = \tanh\left(1.3\,\frac{HS_{\text{pseudo-min}}}{\sigma_{HS_{\text{max}}}^{\text{Helbig}}}\right). \tag{5}$$

Here, $HS_{\text{pseudo-min}}$ is the current HS value or a recent minimum (pink dots in Figure 1a), and $\sigma_{HS_{\text{max}}}^{\text{Helbig}}$ is computed using the current seasonal maximum snow depth HS_{max}, i.e. including the tracking of the maximum in HS and SWE over the course from the start of the season , is applied per grid cell of adistributed snow cover model.

Over the course of the season we describe the $fSCA$ curve by means of one seasonal $fSCA$ ($fSCA_{\text{season}}$) and one $fSCA$ for snowfall events ($fSCA_{\text{nsnow}}$up to the current time step (green dots in Figure 1a). This is done to ensure that a snowfall may add significantly to We call $HS_{\text{pseudo-min}}$ a pseudo-minimum as it is not the absolute seasonal minimum. At each time step, $HS_{\text{pseudo-min}}$ and HS_{max} are updated to compute $fSCA$(. Note that after the PoW, HS_{max} and $\sigma_{HS_{\text{max}}}^{\text{Helbig}}$ remain constant.

For the rare, completely flat grid cells, i.e. $fSCA_{\text{nsnow}} > fSCA_{\text{season}}$) but, once the new snow has started to melt, $fSCA$ can return to similar $fSCA$ values than before. For computing the different $fSCA$ we a subgrid mean slope angle of zero, Eq. (3) would always result in $fSCA = 1$. In those cases, we therefore use Eq. (1) but different HS values (from current to extremes) as well as σ_{HS}, i.e. $\sigma_{HS}^{\text{topo}}$ 4) instead of Eq. (3) to compute $fSCA_{\text{season}}$.

$fSCA_{\text{nsnow}}$

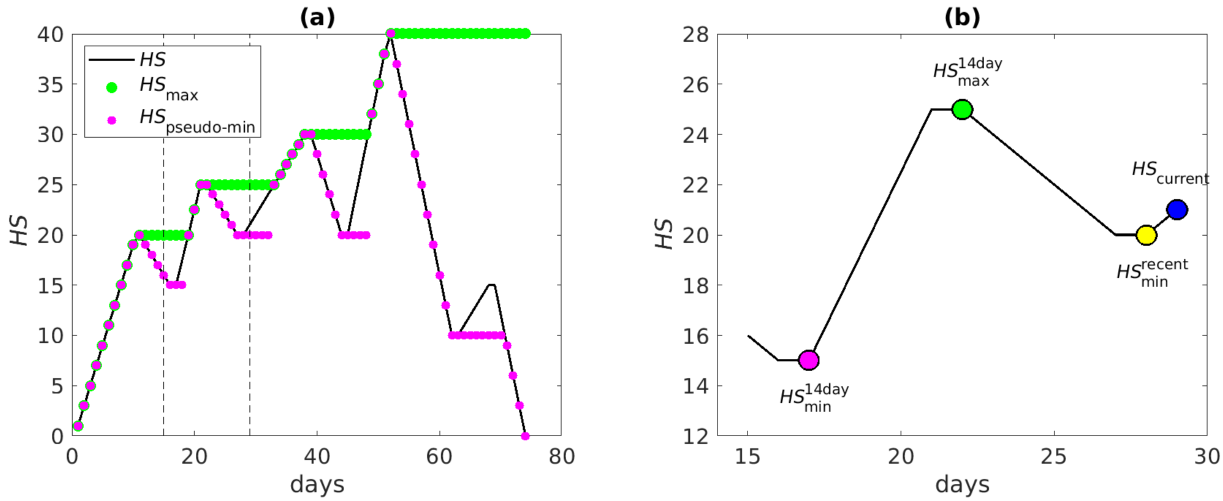

Figure 1. Schematic representation of snow depth HS extreme values used to compute $fSCA$ for a grid cell. (a) To determine $fSCA_{\text{season}}$, extremes in HS (black line) are tracked over the entire season. When HS decreases, the seasonal maximum snow depth HS_{max} (green dots) remains constant until a new maximum is reached with subsequent snowfalls. The pseudo-minimum $HS_{\text{pseudo-min}}$ (pink dots) decreases when HS decreases, until the next snowfall. It then remains constant until HS either exceeds HS_{max} or decreases below the previous minimum. (b) To determine $fSCA_{\text{nsnow}}$, several extremes in HS (black line) are tracked within the last 14 days (black dashed lines in a): the current value HS_{current} (blue dot), the minimum within the last 14 days $HS^{\text{14day}}_{\text{min}}$ (pink dot), the maximum within the last 14 days $HS^{\text{14day}}_{\text{max}}$ (green dot), and the minimum prior to the most recent snowfall $HS^{\text{recent}}_{\text{min}}$ (yellow dot).

To account for possible increases in $fSCA$ after recent snowfalls, we evaluate $fSCA$ (Eq. ~~(2)) or $\sigma^{\text{flat}}_{HS}$ (Eq. (3)) (cf. box in the middle~~ 1) using $\sigma^{\text{Egli}}_{HS}$ (Eq. 4) computed with differences in snow depth dHS (only positive changes) within the last 14 days (Figure 1b). We use dHS rather than HS to only account for the contribution of new snow on changes in $fSCA$, thus as if the new snow fell on bare ground. A time window of 14 days provided reliable $fSCA$ results after intensive testing, but the length of this period may require further investigation once more is known about changes in snow depth distributions in mountainous terrain after snowfall.

Within the 14 day time window, we compute two different $fSCA$ values and then retain the maximum value. First, we evaluate $fSCA^{\text{14day}}_{\text{nsnow}}$ using the largest positive change in snow depth within the last 14 days:

$$fSCA^{\text{14day}}_{\text{nsnow}} = \tanh\left(1.3\,\frac{(HS_{\text{current}} - HS^{\text{14day}}_{\text{min}})}{\sigma^{\text{Egli}}_{dHS^{\text{14day}}}}\right). \tag{6}$$

Here, HS_{current} is the snow depth at the current time step (blue dot in Figure 1b), $HS^{\text{14day}}_{\text{min}}$ is the minimum snow depth in the last 14 days (pink dot in Figure 1b), and $\sigma^{\text{Egli}}_{dHS^{\text{14day}}}$ is computed using the maximum difference in snow depth $dHS^{\text{14day}} = HS^{\text{14day}}_{\text{max}} - HS^{\text{14day}}_{\text{min}}$ in the last 14 days, with $HS^{\text{14day}}_{\text{max}}$ the maximum snow depth in the last 14 days (green dot in Figure 1b).

Table 1. Details of the different $fSCA$ algorithms that are compared to the full $fSCA$ algorithm in $\mathrm{JIM_{OSHD}}$.

algorithm name	$fSCA_{\mathrm{season}}$	$fSCA_{\mathrm{nsnow}}$	tracking HS & SWE (Section 2.2)
$\mathrm{JIM_{OSHD}}$	Eq. (5)	Eq. (6) & (7)	season & 14 days
$\mathrm{JIM_{OSHD}^{season}}$	Eq. (5)	-	season
$\mathrm{JIM_{OSHD}^{curr}}$	$\tanh(1.3\,\frac{HS_{\mathrm{current}}}{\sigma^{\mathrm{Helbig}}_{HS_{\mathrm{current}}}})$	-	-
$\mathrm{JIM_{OSHD}^{allHelbig}}$	Eq. (5)	Eq. (6) & (7) with $\sigma^{\mathrm{Helbig}}_{HS}$	season & 14 days
$\mathrm{JIM_{OSHD}^{Swenson*}}$	Eq. (8.2) in Lawrence et al. (2018)	Eq. (8.1) in Lawrence et al. (2018)	season & 14 days

Second, we evaluate $fSCA^{\mathrm{recent}}_{\mathrm{nsnow}}$ using only the most recent change in snow depth within the last 14 days:

$$fSCA^{\mathrm{recent}}_{\mathrm{nsnow}} = \tanh(1.3\,\frac{dHS^{\mathrm{recent}}}{\sigma^{\mathrm{Egli}}_{dHS^{\mathrm{recent}}}})\,. \tag{7}$$

Here, $dHS^{\mathrm{recent}} = HS_{\mathrm{current}} - HS^{\mathrm{recent}}_{\mathrm{min}}$ is the change in snow since the most recent snowfall, where $HS^{\mathrm{recent}}_{\mathrm{min}}$ is the minimum snow depth prior to the snowfall (yellow dot in Figure 1). The complete technical aspects of the derivation of all b). $fSCA^{\mathrm{recent}}_{\mathrm{nsnow}}$ avoids spatial discontinuities: Without this implementation, grid cells with $HS > 0$ m prior to a recent snowfall may have a lower $fSCA$ including some pseudocode are given in Appendix ??. value than grid cells where the same amount of new snow has fallen on the bare ground.

Finally, the maximum of $fSCA^{\mathrm{14day}}_{\mathrm{nsnow}}$ and $fSCA^{\mathrm{recent}}_{\mathrm{nsnow}}$ gives $fSCA_{\mathrm{nsnow}}$ for the current time step and a grid cell.

Seasonal algorithm

Over the course of the snow season, we derive $fSCA_{\mathrm{nsnow}}$ and $fSCA_{\mathrm{season}}$ for each time step and grid cell (Figure 2). The final $fSCA$ is obtained from was then obtained by taking the maximum of $fSCA_{\mathrm{nsnow}}$ and $fSCA_{\mathrm{season}}$. both values. This full seasonal $fSCA$ algorithm, i.e. including the tracking of HS and SWE, was implemented in a distributed snow cover model. The code is publicly available on the WSL/SLF GitLab repository (cf. Code availability section). The data sets used to evaluate the performance of this algorithm are described in the next section.

3 Data

3.1 Modelled $fSCA$ and HS maps

We model the snow cover evolution using the JULES investigation model (JIM). JIM is a multi-model framework of physically based energy-balance models solving the mass and energy balance for a maximum of three snow layers (Essery, 2013). While the multi-model framework JIM offers 1701 combinations of various process parameterizations, Magnusson et al. (2015)

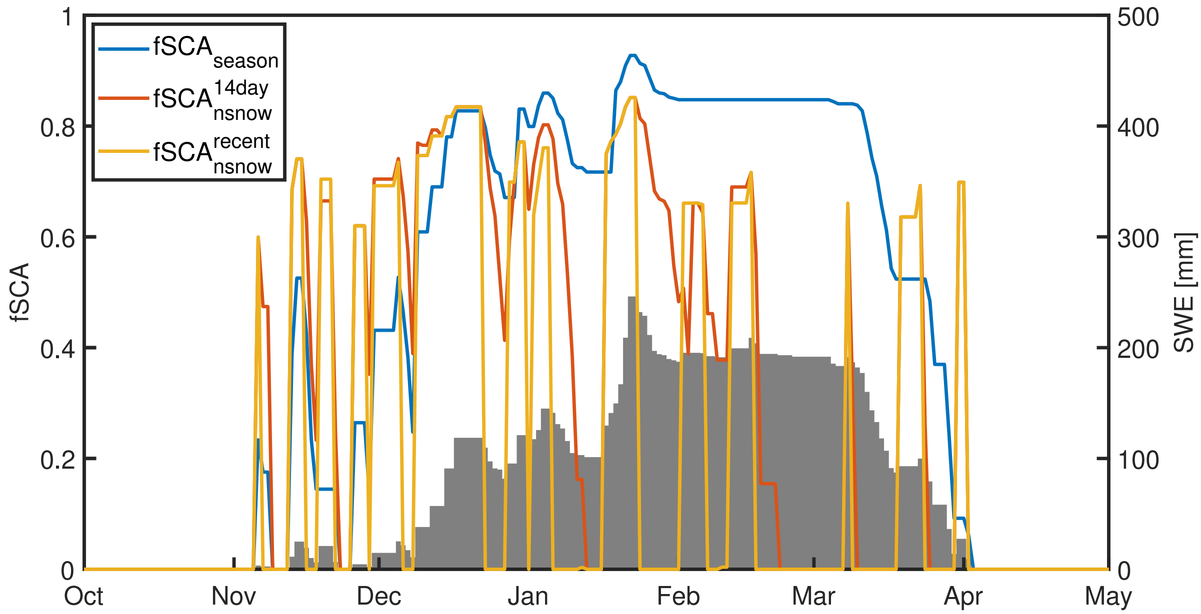

Figure 2. Illustration of modelled $fSCA^{\text{recent}}_{\text{nsnow}}$, $fSCA^{\text{14day}}_{\text{nsnow}}$ and $fSCA_{\text{season}}$ for one grid cell over a season. $fSCA$ is the maximum for each time step from $fSCA_{\text{nsnow}}$=max($fSCA^{\text{recent}}_{\text{nsnow}}$,$fSCA^{\text{14day}}_{\text{nsnow}}$) and $fSCA_{\text{season}}$. All terms are described in Section 2.2.

selected a specific combination that performed best for snow melt modelling for Switzerland~~, predicting~~ . The latter model combination is used to predict daily snow mass and snowpack runoff for the operational snow hydrology service (OSHD) at WSL Institute of Snow and Avalanche Research SLF. We ran JIM_{OSHD} in 1 km resolution with hourly meteorological data from the COSMO-1 model (operated by MeteoSwiss) for Switzerland. We used a reanalysis product of daily observed precipitation (RhiresD) from MeteoSwiss as well as COSMO-1 data. Daily HS measurements from manual observers as well as from a dense network of automatic weather stations (AWS) were used to correct precipitation data via optimal interpolation (OI) (Magnusson et al., 2014), which is a computational efficient data assimilation approach. Using OI in JIM_{OSHD}, Griessinger et al. (2019) obtained improved discharge simulations in 25 catchments over four hydrological years.

To describe the subgrid snow cover evolution in mountainous terrain, ~~the~~ our seasonal $fSCA$ algorithm was implemented in JIM_{OSHD}. As daily values~~we use~~ , we used model output generated at 6 am (UTC). In the following, ~~when we refer to~~ modelled $fSCA$ and HS maps ~~we mean~~ refer to daily $fSCA$ and HS from JIM_{OSHD} model output.

We ~~additionally~~ also computed the snow cover evolution ~~with~~ using JIM_{OSHD} ~~using two~~ with various simplifications in the seasonal $fSCA$ algorithm ~~(Figure 1). Both simplifications are used in coarse-scale model applications and allow us here to estimate the relevance of applying the full seasonal~~ as well as with the $fSCA$ ~~algorithm. First, we switched off all new snow~~ parameterizations implemented in CLM5.0 (Lawrence et al., 2018) which are based on Swenson and Lawrence (2012) (cf. Table 1 for more details). This latter $fSCA$ ~~updates~~algorithm also accounts for hysteresis in accumulation and ablation by using two different $fSCA$ parameterizations and by tracking the seasonal maximum SWE. While subgrid topography is accounted for in the $fSCA$ parameterization during ablation via σ_z, topography is not accounted for during snowfall events. The algorithm of Swenson and Lawrence (2012) was derived by linking daily satellite-retrieved $fSCA$ to snow data. We implemented this algorithm in JIM using our snow tracking algorithm, i.e. the ~~final $fSCA$ was set to $fSCA_{\text{season}}$. Second, we defined a $fSCA_{\text{curr}}$ which only uses current modelled~~ corresponding HS ~~in~~ values such as $HS_{\text{pseudo-min}}$ (cf. Section 2.2). This was done to solely evaluate the differences in the $fSCA$ ~~equation (Eq. (1)), i.e. which does not require any HS tracking. We indicate these~~ parameterizations. In total, we performed four additional snow cover simulations~~with~~: $\text{JIM}^{\text{season}}_{\text{OSHD}}$~~and~~, $\text{JIM}^{\text{curr}}_{\text{OSHD}}$, $\text{JIM}^{\text{allHelbig}}_{\text{OSHD}}$ and $\text{JIM}^{\text{Swenson*}}_{\text{OSHD}}$ (cf. Table 1).

3.2 Evaluation data

3.2.1 ADS fine-scale HS maps

We used fine-scale spatial HS maps gathered by airborne digital scanning (ADS) with an opto-electronic line scanner on an airplane. Data were acquired over the Wannengrat and Dischma area near Davos in the eastern Swiss Alps during winter and summer (Bühler et al., 2015). We used ADS-derived HS maps at three points in time during one winter season, namely during accumulation ~~at~~ on 26 January ('acc'), at approximate peak of winter ~~at~~ on 9 March ('PoW') and during ablation season ~~at~~ on 20 April 2016 ('abl') (Marty et al., 2019). We used a summer DEM from ADS to derive the snow-free terrain parameters.

Each ADS data set covers about 150 km^2 with 2 m spatial resolution. Compared to terrestrial laser scan (TLS)-derived HS data~~of a subset~~, the 2 m ADS-derived HS maps had a root mean square error (RMSE) of 33 cm and a normalized median absolute deviation (NMAD) ~~of the residuals (Höhle and Höhle, 2009)~~ of 24 cm (Bühler et al., 2015).

3.2.2 ALS fine-scale HS maps

We used fine-scale spatial HS maps gathered by airborne laser scanning (ALS). The ALS campaign was a Swiss partner mission of the Airborne Snow Observatory (ASO) (Painter et al., 2016). Lidar setup and processing standards were similar to those in the ASO campaigns in California. ~~The data was~~ Data were acquired over the Dischma area near Davos in the eastern Swiss Alps (cf. Figure 3a in Helbig et al., 2021). We used ALS-derived HS maps at three points in time during one winter season, namely at ~~approximate time of~~ the approximate peak of winter ~~at~~ on 20 March ('PoW') and during the early and late-ablation season ~~at~~ on 31 March and 17 May 2017 ('abl'), respectively. We used a summer DEM from ALS from 29 August 2017 to derive the ~~summer~~ snow-free terrain parameters.

Each ALS data set ~~covers~~ covered about 260 km^2. The original 3 m resolution was aggregated to 5 m horizontal resolution. ~~A RMSE of 13 cm and a bias of -5 cm with snow probing was obtained for~~ Comparing the ALS-derived HS data to manual snow probing within forest but outside canopy (i.e. not below a tree)~~1 m ALS-derived HS data from~~, Mazzotti et al. (2019) reported a RMSE of 13 cm and a bias of -5 cm for 20 March ~~2017 (Mazzotti et al., 2019).~~ 2017.

3.2.3 Terrestrial camera images

We used camera images from terrestrial time-lapse photography in the visible band. The camera (Nikon Coolpix 5900 from 2016 to 2018, Canon EOS 400D from 2019 to 2020) was installed at the SLF/WSL in Davos Dorf in the eastern Swiss Alps (van Herwijnen and Schweizer, 2011; van Herwijnen et al., 2013). Photographs were taken of the Dorfberg in Davos, which is a large southeast-facing slope with a mean slope angle of about 30° (cf. Figure 1 in Helbig et al., 2015a). To obtain $fSCA$ values from the camera images, we followed the workflow described by Portenier et al. (2020). We used the algorithm of Salvatori et al. (2011) to classify pixels in the images as snow or ~~snow free~~snow-free. Though images are taken at regular intervals (between 2 and 15 minutes, depending on the year), we used the image at noon to derive $fSCA$ for that day. We evaluated images from five winter seasons (2016, 2017, 2018, 2019 and 2020) ~~each~~ every time from 1 November ~~until~~ to 30 June.

The resulting snow/~~no snow~~ no-snow map of the camera images ~~has~~ had a horizontal resolution of 2 m. The field of view (FOV) overlaps ~~the most~~ with four 1 x 1 km JIM_{OSHD} grid cells with projected visible fractions between 9 to 40 % in each grid cell. The camera ~~data set can thus cover roughly~~ FOV covers about 0.76 km^2~~per time step~~.

3.2.4 Sentinel-2 snow products

We used fine-scale snow-covered area maps ~~, which we~~ obtained from the Theia snow collection (Gascoin et al., 2019). The satellite snow products were generated from Sentinel-2 L2A and L2B images. We used Sentinel-2 snow-covered area maps over one winter season ~~starting at~~ from 20 December 2017 ~~until~~ to 31 August 2018 for Switzerland. We further used Sentinel-2 snow maps over the Dischma area near Davos close to or at the date of the three ~~days when we had ALS-derived $fSCA$ maps available~~ ALS-scans (18 and 28 March and 17 May 2017) ~~.~~ and over the Dorfberg area in Davos Dorf from 1 November 2017 to 30 June 2018.

The horizontal resolution of the snow product is 20 m. While the spatial coverage of the Sentinel-2 snow-covered area maps in Switzerland varies every time step, Sentinel-2 may cover several ~~thousands of square kilometersper time step~~thousand square kilometers. A validation of the Theia snow product with snow depth from AWS, through comparison to snow maps with higher spatial resolution as well as by visual inspection indicated that snow is ~~detected very well though with~~ well detected, although there is a tendency to underdetect snow (Gascoin et al., 2019). The main difficulty of satellite snow products is to avoid false snow detection within clouds. Furthermore, snow omission errors may occur on steep, shaded slopes when the solar elevation is typically below 20°.

3.3 Derivation of 1 km $fSCA$ evaluation data

For ~~preprocessing~~pre-processing, we masked out forest, rivers, glaciers or buildings in all fine-scale measurement data sets. Optical snow products that were obscured by clouds were also neglected. In all fine-scale HS data sets, we neglected HS values that were lower than zero or above 15 m. We used a HS threshold of zero m to decide whether or not a 2 or 5 m grid cell was snow-covered. This threshold could not be better adjusted due to a lack of independent ~~spatial~~ observations. ~~This likely~~

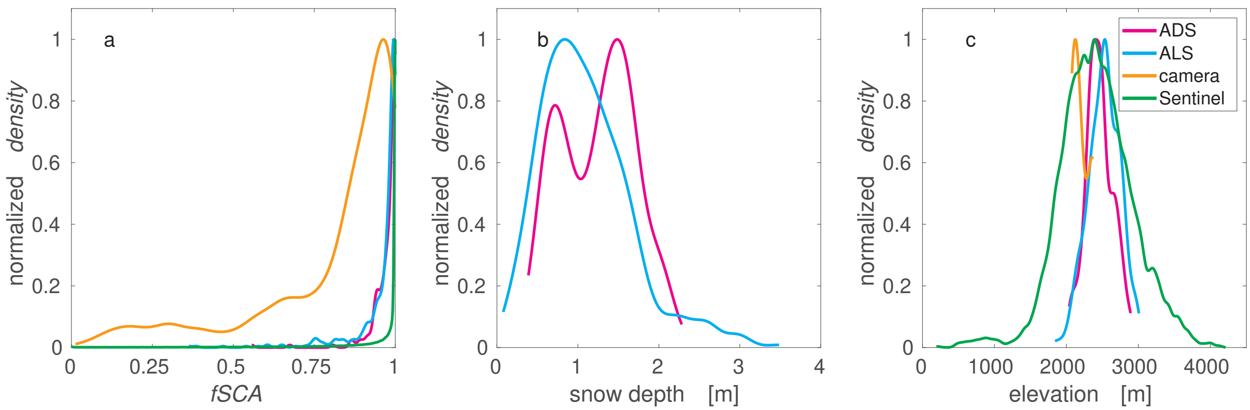

Figure 3. Probability density functions after preprocessing for all valid 1 km (a) $fSCA$, (b) HS snow depth and (c) elevation z per measurement data set. All densities were normalized with the maximum in each data set. Colors represent the different measurement platforms as detailed in Section 3.2.

led to the rather narrow $fSCA$ peak of the probability density function (pdf) around one (cf. pink and light blue line in Figure 2).

We then aggregated all fine-scale snow data, as well as the snow products from optical imagery, in squared domain sizes L in regular grids of 1 km aligned with the OSHD model domain. For building the spatial averages, we required at least 70 % valid data for the fine-scale snow data and at least 50 % valid for the satellite-derived $fSCA$ data in a domain size L of each 1 km grid cell. We excluded 1 km domains grid cells with spatial mean slope angles larger than 60° and spatial mean measured HS lower than or modelled HS $<$5 cm. We further neglected 1 km grid cells with forest fractions larger than 10 %, which were derived from 25 m forest cover data. Overall, this led to a varying number of available domains in variable number of 1 km valid grid cells for the different data sets (Table 12). For the fine-scale snow data sets, this number ranged from 69 to 157 available valid 1 km domains depending on the point in time with a total of 669 668 valid 1 km domains. After the removal of clouds and forest we obtained on averagegrid cells. After cloud and forest removal, on average, every second day in Switzerland we had some valid Sentinel-2 data in Switzerland (153 valid days from the 255 calendar days). For the time period from 20 December until 2017 to 31 August 2018, this resulted in 274'979 216'896 valid 1 km domains grid cells from a total of 3'147'465 2'274'991 valid OSHD grid cells in Switzerland, i.e. about 9 9.5 %. These valid 1 km domains cover terrain elevations between grid cells covered terrain elevations from 174 m and 4213 m, slope angles between to 4278 m, subgrid mean slope angles from 0 to 5260 and all terrain aspects. We used three of the four grid cells covered by the FOV of the terrestrial camera, since one grid cell had a 1 km forest fraction larger than 10 %. On averagewe obtained , every fourth day we had valid camera data (340 337 valid days from 1211 the 1212 calendar days). Valid camera-derived $fSCA$ for five seasons and the three grid cells covered by the FOV resulted in 1'019 931 valid 1 km grid cells from a total of 3'633 1 km grid cells for the five seasons and three 018 valid OSHD grid cells, i.e. 28 %. Compared to the total of all valid OSHD grid cells in Switzerland for the five seasons, the fraction of valid camera-derived $fSCA$ is however less than 0.01 %. 31 %. The three grid

Table 2. Details of the valid 1 km $fSCA$ evaluation data sets after pre-processing as described in Section 3.3.

geographical region	remote sensing method	spatial ~~resolution~~ coverage ~~(fine-scale)~~	~~spatial~~ temporal coverage	σ_{fSCA}	mean $fSCA$
		[~~m~~km^2]	[days]		
Wannengrat and Dischma area (eastern CH)	ADS	~~2~~ 232	3	0.05	0.98
Dischma and Engadin area (eastern CH)	ALS	~~3 437~~ 436	3	0.08	0.96
Davos Dorfberg (eastern CH)	Terrestrial camera	~~2 1'019~~ 931	~~340~~ 337	~~0.30~~ 0.23	~~0.75~~ 0.81
Switzerland	Sentinel-2	~~20 274'979~~ 216'896	153	~~0.46~~ 0.18	~~0.54~~ 0.93

cells have terrain elevations of 2077 m, 2168 m and 2367 m and slope angles of 27°, 34° and 39°. The diversity in each of the evaluation data sets after ~~preprocessing~~ pre-processing is indicated in Table ~~1~~ 2 and is also shown for valid 1 km domains by means of the pdf for $fSCA$, HS and terrain elevation z in Figure ~~2~~3.

3.4 Performance measures

~~We evaluate modelled and measured~~ To evaluate the performance of modelled $fSCA$ ~~with the following~~ compared to the measurements, we used three measures: the root mean square error (RMSE), the normalized root mean square error (NRMSE~~,~~ ; normalized by the mean of the measurements) ~~, mean absolute error (MAE)~~ and the mean percentage error (MPE~~, bias with~~ ; defined as measured minus modelled~~and normalized with measurements). We also verify distribution differences by deriving the two-sample Kolmogorov-Smirnov test (K-S test) statistic values D (Yakir, 2013) for the probability density functions (pdf) and by computing the NRMSE for Quantile-Quantile plots (NRMSE$_{quant}$, normalized by~~ , normalized with the mean of the ~~measured quantiles)for probabilities with values in $[0.1, 0.9]$.~~

measurements).

4 Results

We ~~grouped the evaluation results of the~~ present the evaluation of our seasonal $fSCA$ algorithm in three sections: evaluation with $fSCA$ derived from fine-scale HS maps near Davos, evaluation with $fSCA$ from time-lapse photography in Davos Dorf and evaluation with $fSCA$ from Sentinel-2 snow products ~~. Modelled $fSCA$ (JIM$_{OSHD}$) and ADS-derived $fSCA$ in elevation bins for three dates: (a) during accumulation, (b) at approximate peak of winter (PoW) and (c) during ablation. Two benchmarks are shown where applicable. The red stars were derived using Eq. (1) with current ADS HS in the numerator and ADS σ_{HS} from the PoW measurement in the denominator. The blue stars were derived using Eq. (1) with current ADS HS in the numerator and current ADS σ_{HS} in the denominator. The bars show the valid data percentage per bin.~~over Switzerland. We further present some additional comparisons with Sentinel-2 snow products in the first two sections when Sentinel-2 data was available in the Davos area (cf. Section 3.2.4).

Table 3. Performance measures ~~are shown~~ for modelled $fSCA$ with (I) $fSCA$ derived from all fine-scale HS maps (combined ADS- and ALS-derived $fSCA$) and (II) Sentinel-derived $fSCA$ (only available for ALS dates). ~~Performance~~ Additionally, performance measures are shown for ALS-derived $fSCA$ with Sentinel-derived $fSCA$ (III) and for modelled $fSCA$ using $JIM_{OSHD}^{Swenson*}$ (IV). Given statistics are NRMSE, RMSE ~~, MPE, MAE, K-S test statistic~~ and ~~$NRMSE_{quant}$~~ MPE. For all differences we computed measured minus modelled values respectively Sentinel-derived $fSCA$ minus ALS-derived $fSCA$ for III. The ~~abbreviations 'acc', 'PoW' and 'abl' indicate the~~ different ~~point~~ points in time of the season ~~as given~~ are specified in Section 3.2.

$fSCA$	NRMSE	RMSE	MPE ~~MAE K-S $NRMSE_{quant}$~~
	[%]		[%] ~~%~~
I JIM_{OSHD} vs ADS&ALS			
~~$fSCA$ 8.5 0.08 1.2~~ all dates	~~0.04~~ 7	~~0.27~~ 0.07	~~1.0~~ 0.7
~~$fSCA_{acc}$~~ accumulation date	~~8.0~~ 8	0.08	~~-3.6 0.04 0.46 3.2~~ -3.8
~~$fSCA_{PoW}$ 4.9 0.05~~ PoW dates	~~0.6~~ 2	0.02	~~0.50 0.7~~ 0.3
~~$fSCA_{abl}$ 10.4 0.10 2.4~~ ablation dates	~~0.05~~ 8	~~0.20~~ 0.08	~~2.6~~ 1.8
II JIM_{OSHD} vs Sentinel-2 (at ALS dates)			
~~$fSCA$ 10.1 0.09 -0.5~~ all dates	~~0.05~~ 9	~~0.24~~ 0.08	~~2.9~~ -1.4
~~$fSCA_{PoW}$~~ PoW dates	~~2.8~~ 3	0.03	2.5 ~~0.03 1 2.7~~
~~$fSCA_{abl}$ 10.2 0.09 -0.6~~ ablation dates	~~0.05~~ 9	~~0.22~~ 0.08	~~2.9~~ -1.5
III Sentinel-2 vs ALS			
~~$fSCA$~~ all dates	~~10.8~~ 11	0.10	3.1
PoW date	~~0.05~~ 9	0.08	-5.9
ablation dates	11	0.10	~~4.6~~ 3.4
~~$fSCA_{PoW}$~~ height IV $JIM_{OSHD}^{Swenson*}$ vs ADS&ALS	~~8.7~~	~~0.08~~	
all dates	~~-5.9~~ 14	~~0.06~~ 0.14	~~1~~ -1.2
accumulation date	~~7.7~~ 9	0.09	-6.1
~~$fSCA_{abl}$~~ PoW dates	~~10.9~~ 6	~~0.10~~ 0.06	~~3.4~~ -0.6
ablation dates	~~0.05~~ 18	~~0.11~~ 0.18	~~4.8~~ -0.7

4.1 Evaluation with $fSCA$ from fine-scale HS maps

Modelled $fSCA$ compares very well to compared well with $fSCA$ derived from all six fine-scale HS data sets. For instance for all evaluated points in time we obtain Overall, we obtained a NRMSE of 9 %7 %, a RMSE of 0.07 and a MPE of 1 0.7 % (Table 2). Overall best performances are achieved for the combined 3). The best performance was for the two dates at the approximate date of PoW with a NRMSE of 5 %PoW (NRMSE of 2 %, a RMSE of 0.02 and a MPE of 0.6 %. The performance decreases slightly for the accumulation date (NRMSE of 8 %)and the combined three points in time of ablation (NRMSE of 10 %)0.3 %), while the performance was somewhat lower during the ablation and accumulation period.

Given the overall good seasonal agreement between $fSCA$ from all fine-scale HS data sets and modelled $fSCA$

To investigate the influence of elevation, we binned the data in 200 m elevation bands and for for the ADS and ALS data sets separately to unveil seasonal variations in the elevation-dependent performances. Similar to overall seasonal model performances (Table 2, I), seasonal elevation-dependent performances with ALS data decrease from PoW, to ablation(Figures 4 and 5). For ADS data, seasonal elevation-dependent performances are similar good modelled $fSCA$ values were comparable to the measurements at PoW and early ablationand decrease during accumulation . Except for the date during accumulation , largest performance differences occur mostly for the lowest elevationbin, i.e. in general, model performances improve with elevation. While at both early ablation dates there is still an overall good agreement between HS-derived $fSCA$ and , while the differences during accumulation were more pronounced (compare red and black dots in Figure 4). There was also no consistent elevation trend, as during accumulation differences between modelled and measured $fSCA$ increased with elevation, while during early ablation the opposite was true. For the ALS data, measurements were only available at PoW and during ablation. Overall, modelled $fSCA$ (red versus values were again in line with the measurements (compare red and black dots in Figure 3c and 4b), at the ablation date modelled $fSCA$ underestimates ALS-derived $fSCA$ across all elevations (Figure 4c5). The largest underestimations occur for the two lowest elevation bins with each on average 0.14. Across all elevations, we obtain almost consistently good performances at approximate PoW (Figure 3b and 4a). Larger overestimations occur only at lowest elevations between 1700 m and 1900 m with on average 0.15. At the date during accumulation, performances decrease with elevation. Modelled difference was observed for the lowest elevation bin (0.15 at PoW at 1800m; Figure 5a), and for the late ablation data, modelled $fSCA$ overestimates ADS-derived was consistently lower than ALS-derived $fSCA$at elevations above 2100 m with at maximum 0.09 (Figure 3a). , in particular for the lower elevation bins (Figure 5c).

Modelled $fSCA$ (JIM_{OSHD}), ALS-derived $fSCA$ and Sentinel-derived $fSCA$ in elevation bins for three dates: (a) at approximate PoW, (b) during early ablation and (c) during late ablation. The same two benchmarks as indicated in Figure 3 are shown where applicable. Sentinel-derived $fSCA$ was available 2 days before the PoW, 3 days before the early ablation and at the point in time of the late ablation ALS flight date (green line). The bars show the valid data percentage per bin.

Modelled snow depth HS (JIM_{OSHD}) and ADS-derived HS in elevation bins for three dates: (a) during accumulation, (b) at approximate PoW and (c) during ablation.Modelled snow depth HS (JIM_{OSHD}) and ALS-derived HS in elevation bins for three dates: (a) at approximate PoW, (b) during early ablation and (c) during ablation.

Some valid Valid Sentinel-2 coverage is available at or data were only available on dates close to the dates of the ALS measurements . Though overall seasonal performances between ALS measurements (green dots in Figure 5), not to the ADS measurement dates. Overall, modelled and Sentinel-derived $fSCA$ decrease from PoW to the combined two ablation dates (Table 2, II), seasonal elevation-dependent performances are best across all elevations for the latest ablation date when Sentinel-2 coverage is available at the exact same day (green versus values were in good agreement for the three ALS dates (II in Table 3), there was no clear elevation dependence (compare green and red dots in Figure 4). At the lowest binned elevations between 1700 m and 1900 m and between 1900 m and 2100 m modelled $fSCA$ underestimates Sentinel-derived $fSCA$ with on average respectively 0.03 and 0.04 (Figure 4b and 5), and differences were at most 0.05 (for elevations between 2300 m and 2500 m in Figure 5c). Seasonal performances between Sentinel- and ALS-derived $fSCA$ across all elevations are similar to the performances between modelled and ALS-derived $fSCA$. For all dates with Sentinel-2 coverage we obtain similar NRMSE. Between modelled and The Sentinel-derived $fSCA$ the NRMSE is 10 % and between Sentinel- values can also be compared to those from the ALS scans. In this case, the performance measures were somewhat lower (compare II and III in Table 3), and ALS-derived $fSCA$ the NRMSE is 11 % (Table 2, II versus III).

To understand modelled Sentinel-derived $fSCA$ performances we also evaluated modelled with measured HS in 200 m - elevation bins (see Figure 5 and 6). Compared to the seasonal snow depth change between the three dates of ADS-HS (Figure 5) there is much less seasonal variation than between the three dates of the ALS-HS data across all elevations (Figure 6). While on the one hand, the time intervals are much smaller between the three dates of the ALS acquisitions (20 March, 31 March, 17 May 2017) compared to the ones of the ADS acquisitions (26 January, 9 March and 20 April 2016), there were also some snowfall events during ablation in 2017. Except for at the date during accumulation performances decrease with elevation starting at elevations of about 2100 m to 2500 m. Modelled HS considerably underestimates measured HS at higher elevations while at lower elevations modelled HS mostly overestimates measured HS, except for the accumulation and PoW date of the ADS data. Seasonal performances do not show a clear trend, but best performances are achieved during accumulation. For all dates and data sets, modelled HS shows a NRMSE of 12 % and a MPE of 14 % with measured HSvalues were especially lower than the ALS data in late ablation (compare green and black dots in Figure 5c).

The

Our seasonal $fSCA$ algorithm was is implemented in a complex operational snow cover model framework (Section 3.1). Uncertainties related to input or model structure may therefore have an impact on therefore impact modelled HS and thus $fSCA$ performances. We investigated this by deriving values. To investigate the influence of these uncertainties more closely, we also derived two benchmark $fSCA$ with models based on Eq. (1) using measured rather than modelled HS dataonly. The first benchmark $fSCA$ uses current observed σ_{HS} and $fSCA^{\text{measured}}_{\text{curr}}$ (light blue stars in Figures 4 and 5) uses measured HS , namely a $fSCA^{\text{measured}}_{\text{curr}}$and σ_{HS} from the current scan. The second benchmark model combines current measured HS and observed σ_{HS} at PoW, namely a $fSCA^{\text{measured}}_{\text{PoW}}$ (cf. blue and red stars in Figure 3 and 4). orange stars in Figures 4 and 5) combines current HS measurements with σ_{HS} values measured at PoW. At PoW, $fSCA^{\text{measured}}_{\text{PoW}}$ and $fSCA^{\text{measured}}_{\text{curr}}$ are the same, and $fSCA^{\text{measured}}_{\text{PoW}}$ can only be derived when PoWhas passed, i.e. during ablation. at or after PoW. Overall performances of both benchmark Results obtained with both benchmark models were similar, except for the lowest elevation bin in the

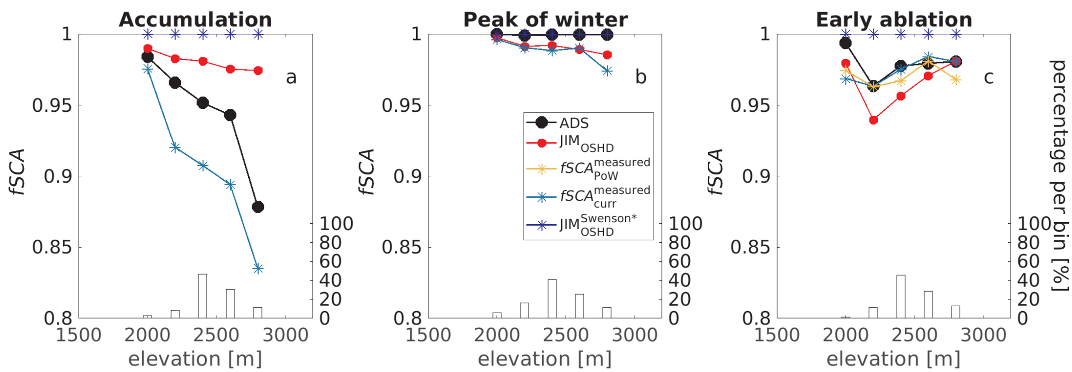

Figure 4. Modelled and ADS-derived $fSCA$ in 200 m elevation bins for three dates: (a) during accumulation, (b) at approximate peak of winter (PoW), and (c) during ablation. Two benchmarks based on Eq. (1) are shown where applicable: $fSCA^{\text{measured}}_{\text{PoW}}$ (orange stars) uses HS form the current ADS scan and σ_{HS} from the ADS scan at PoW, while $fSCA^{\text{measured}}_{\text{curr}}$ (light blue stars) uses HS and σ_{HS} form the current ADS scan. The bars show the valid data percentage per bin.

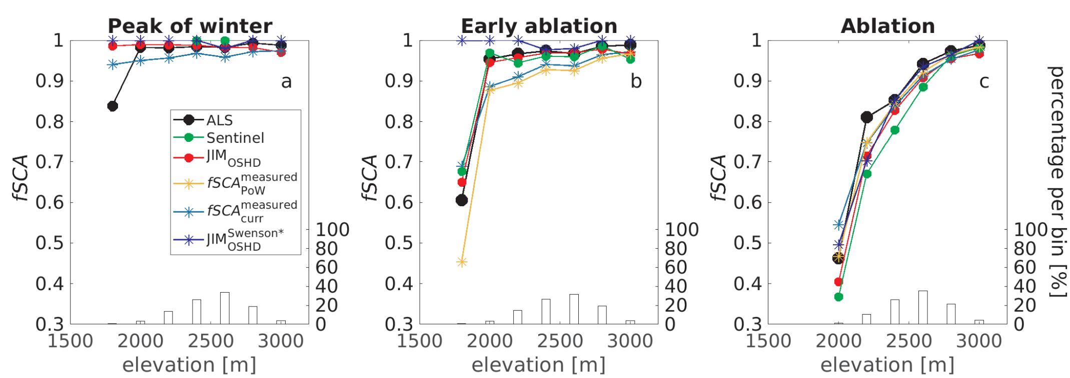

Figure 5. Modelled and ALS-derived, and Sentinel-derived $fSCA$ in 200 m elevation bins for three dates: (a) at approximate PoW, (b) during early ablation and (c) during late ablation. The same two benchmarks based on Eq. (1) as in Figure 4 are also shown where applicable. Sentinel-derived $fSCA$ (green dots) was available 2 days before the PoW scan, 3 days before the early ablation scan and on the same day as the late ablation scan. The bars show the valid data percentage per bin.

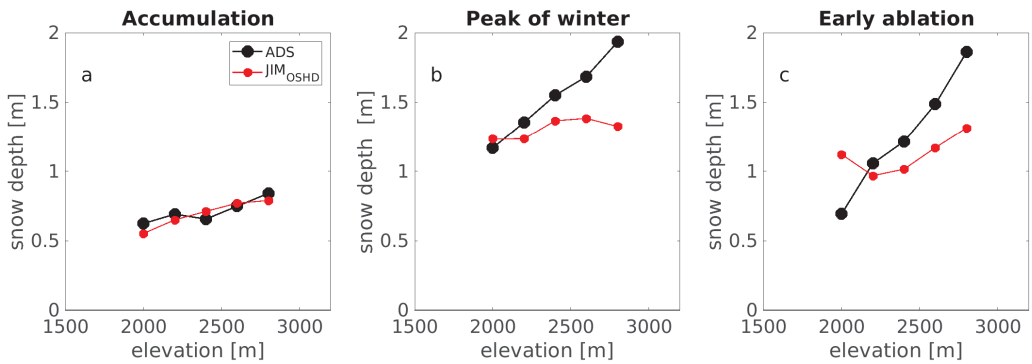

Figure 6. Modelled and ADS-derived HS in 200 m elevation bins for three dates: (a) during accumulation, (b) at approximate PoW and (c) during ablation.

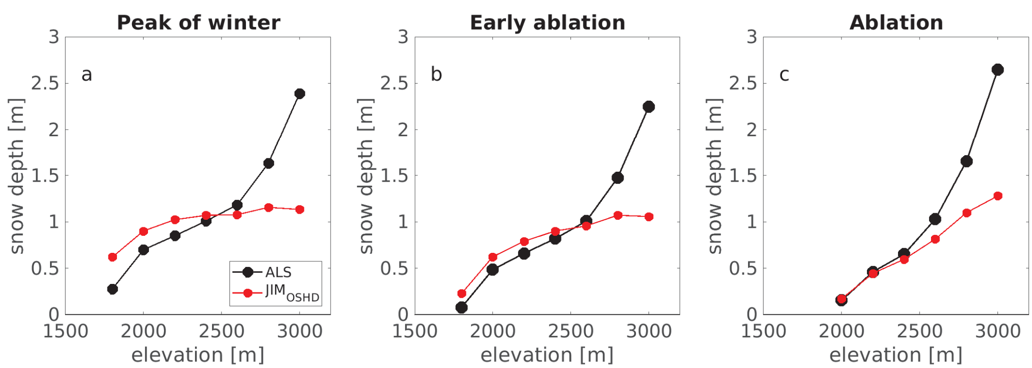

Figure 7. Modelled and ALS-derived HS in 200 m elevation bins for three dates: (a) at approximate PoW, (b) during early ablation and (c) during ablation.

ALS data set (Figure 5b and c). Overall, the values of $fSCA^{\text{measured}}_{\text{curr}}$ were somewhat closer to the measured $fSCA$ are better (lower NRMSE) compared to modelled $fSCA$. Among all dates, best seasonal elevation-dependent performances (200 m bins)of $fSCA^{\text{measured}}_{\text{curr}}$ and $fSCA^{\text{measured}}_{\text{PoW}}$ are achieved for two of the ablation dates (red and values (e.g. Figure 4c or 5b). Both benchmark models were closest to the measured $fSCA$ values during the ablation season (Figure 4c and 5c), and overall the agreement was better for higher elevation bins. Our seasonal $fSCA$ implementation (red dots in Figures 4 and 5) was also similar to both benchmark models. The largest differences were during the accumulation period (Figure 4a).

As a final benchmark, we also compared our seasonal $fSCA$ implementation with the parameterizations implemented in CLM5.0 (cf. Table 1). Modelled $fSCA$ using JIM$_{\text{OSHD}}$ performed better than that modelled with JIM$^{\text{Swenson*}}_{\text{OSHD}}$ (compare I and IV in Table 3). During most of the season, $fSCA$ values from JIM$^{\text{Swenson*}}_{\text{OSHD}}$ were close to 1 and showed little elevation dependence (blue stars in Figure 3c and 4 c). Performances mostly improve, similarly to as for modelled 4 and 5). The only exception was during the late-ablation season, when $fSCA$, with elevation . For the three ablation dates , we obtain overall similar

~~NRMSE 's for both benchmark models. Except for the lowest elevation bin seasonal elevation-dependent performances are also similar among both benchmark models though the performance of $fSCA^{\text{measured}}_{\text{curr}}$ is slightly improved (e.g. Figure 3c or 4b~~from JIM_{OSHD} and from $\text{JIM}^{\text{Swenson*}}_{\text{OSHD}}$ were very similar (blue and red dots in Figure 5c).

To investigate the origin of the discrepancies between modelled and observed $fSCA$ values more closely, we compared modelled and measured HS in 200 m elevation bins for the ADS and ALS data sets separately (Figure 6 and 7). For both data sets, modelled HS was substantially lower than measured HS at higher elevations. The only exception was for the accumulation date, when modelled and measured HS were in good agreement for all elevations (Figure 6a). For all dates and data sets, the NRMSE between modelled and measured HS was 12 % and the MPE was 14 %. Note that seasonal variations in ALS-HS across all elevations were generally much lower than those in the ADS-HS data. This was in part because the time intervals between the three ALS scans (20 March, 31 March, 17 May 2017) were shorter than for the ADS scans (26 January, 9 March and 20 April 2016), and there were also some snowfall events during the ALS ablation period (spring 2017).

4.2 Evaluation with $fSCA$ from camera images

The high temporal resolution of ~~daily~~ camera-derived $fSCA$ ~~allows~~ allowed us to evaluate ~~seasonal model performances. Overall, modelled~~ the seasonal model performance. The seasonal trend in modelled $fSCA$ ~~follows the seasonal trend of~~ using JIM_{OSHD} was generally in line with that from camera-derived $fSCA$ ~~for two of the three grid cells throughout almost all seasons well (cf. for two seasons Figure 7a,c,d,f). However, for~~ (compare red and black dots in Figure 8). For the grid cell at 2168 m, however, the agreement was somewhat poorer, as there was a delay in the modelled start of the ablation season~~starts much later with modelled $fSCA$ compared to camera-derived $fSCA$~~, and modelled $fSCA$ ~~further overestimates camera-derived $fSCA$~~ values were too high during accumulation (Figure ~~7~~8b,e).

For all winter seasons (2016 to 2020~~and~~) and for the three grid cells~~we obtain~~, we obtained a NRMSE of ~~22 %~~21 %, a RMSE of 0.17 and a MPE of -7 % ~~for modelled $fSCA$ (Table 3, I). However, interannual performances vary considerably as well as performances~~ (I in Table 4). Note that the inter-annual performance varied substantially, as did the performance among the three grid cells. For instance, for all three grid cells, ~~we obtain~~ the overall best performance was for the season 2018 ~~with a NRMSE of 15 %and a MPE of~~ (NRMSE = 14 %, RMSE = 0.11, MPE = -4 %~~and the worst performances for~~), while the worst performance was for the season 2019 ~~with a NRMSE of~~ (NRMSE = 25 %~~and a MPE of~~, RMSE = 0.2, MPE = -12 %~~and season 2020 with a NRMSE of 23 % and a MPE of -17 %.~~).

For winter season 2018, we used Sentinel-derived $fSCA$ to evaluate modelled and camera-derived $fSCA$ ~~(Table 3, II and III; Figure 7d,e,f). While~~ values. While overall the agreement between modelled and Sentinel-derived $fSCA$ ~~agree very well (NRMSE of~~ was good (NRMSE 2 % and MPE of ~~-1~~ 1 %), ~~Sentinel- and camera-derived~~ the agreement between camera- and Sentinel-derived $fSCA$ ~~compare less well (NRMSE of~~ was poorer (NRMSE = 12 %~~and MPE of -5 %)though performances are similar to those for~~, MPE = 5 %). The latter performance values were however comparable to the agreement between modelled and camera-derived ~~and modelled~~ $fSCA$ ~~(NRMSE of 15 %and a MPE of~~ for days with valid Sentinel-derived data (NRMSE = 12 %, MPE = -4 %).

We exploited the high temporal resolution of The camera-derived $fSCA$ was also used to evaluate the relevance of applying the our full seasonal $fSCA$ algorithm, as opposed to snow cover model simplifications of the $fSCA$ algorithm, namely $fSCA_{\text{season}}$ and $fSCA_{\text{curr}}$ (JIM$^{\text{season}}_{\text{OSHD}}$ and JIM$^{\text{curr}}_{\text{OSHD}}$simplifications and JIM$^{\text{Swenson*}}_{\text{OSHD}}$ (cf. Table 1 for details). While $fSCA_{\text{season}}$ and modelled overall $fSCA$ agree wellwhen the snow cover is quite homogeneous, after snowfalls from JIM$^{\text{season}}_{\text{OSHD}}$ and JIM$_{\text{OSHD}}$ agreed well, there were substantial differences after snowfall events on partly snow-free ground , $fSCA_{\text{season}}$ can be considerably lower (yellow stars versus (compare orange stars and red dots in Figure 7b,c). When replacing the $fSCA$ algorithm with $fSCA_{\text{curr}}$, deviations to 8). Specifically, after such a snowfall event, modelled $fSCA$ using the full algorithm are getting larger (blue stars versus JIM$_{\text{OSHD}}$ generally increased, while JIM$^{\text{season}}_{\text{OSHD}}$ remained constant. Using JIM$^{\text{curr}}_{\text{OSHD}}$, modelled $fSCA$ values were less in line with those from JIM$_{\text{OSHD}}$ (compare light blue stars and red dots in Figure 7). Large overestimations occur similarly after snowfall but large differences now also occur independent from snowfalls during 8). While discrepancies were again large after snowfall event, they were also pronounced during the ablation periods. The start of ablation season is delayed but is In general, with JIM$^{\text{curr}}_{\text{OSHD}}$ the ablation season started later and was followed by a much steeper melt out compared to the full period. Using JIM$^{\text{curr}}_{\text{OSHD}}$ can result in a substantially shorter snow season compared to JIM$_{\text{OSHD}}$, with a maximum difference of 21 days at 2168 m in the season 2017. Overall, compared to camera-derived $fSCA$model. Applying $fSCA_{\text{curr}}$ always considerably shortens the season compared to applying the full , both simplified models performed less well than JIM$_{\text{OSHD}}$ (Table 4). The performance using JIM$^{\text{allHelbig}}_{\text{OSHD}}$ was very similar to $fSCA$ algorithm. For instance, for season 2016 the shortening is 46 days at 2077 m. In part, $fSCA_{\text{season}}$ also shortened the ablation season compared to the full from JIM$_{\text{OSHD}}$, i.e. applying $\sigma^{\text{Helbig}}_{HS}$ instead of $\sigma^{\text{Egli}}_{HS}$ for $fSCA_{\text{nsnow}}$ did not substantially affect model performance. On the contrary, $fSCA$ algorithm by at maximum 24 days at 2077 m in season 2016 not shown. In season from JIM$^{\text{Swenson*}}_{\text{OSHD}}$ had the worse overall performances when compared to camera-derived $fSCA$ (VII in Table 4). Similar to JIM$^{\text{curr}}_{\text{OSHD}}$, using JIM$^{\text{Swenson*}}_{\text{OSHD}}$ considerably delayed the ablation season, followed by a much steeper melt out. The snow season was substantially shortened again by at most 32 days in the 2017 and 2020 however, applying $fSCA_{\text{season}}$ prolonged the season by at maximum 6 days at 2168 min season 2020. Overall, both simplified season at 2077 m. Modelled $fSCA$ models compare less well to camera-derived using JIM$^{\text{Swenson*}}_{\text{OSHD}}$ also largely overestimates $fSCA$ than modelled during the accumulation period (blue dots in Figure 8). Overall, using JIM$^{\text{Swenson*}}_{\text{OSHD}}$ led to much steeper increases and decreases in $fSCA$using the full , i.e. an almost binary seasonal $fSCA$ trend that was not in line with camera-derived $fSCA$algorithm, however $fSCA_{\text{season}}$ performs better than $fSCA_{\text{curr}}$ (Table 3, I).

4.3 Evaluation with $fSCA$ from Sentinel-2 snow products

Overall, modelled $fSCA$ compares well to using JIM$_{\text{OSHD}}$ compared well with Sentinel-derived $fSCA$ throughout the season , though there is some (I in Table 5). To investigate the elevation-dependent scatter differences between modelled and Sentinel-derived $fSCA$ (Figure 8).

In order to analyze the elevation-dependent scatter between modelled and Sentinel-derived $fSCA$, we derived in more detail, we binned the data in 250 m elevation bands for each day throughout the entire season (Figure 9). To estimate the end of the accumulation (1 April 2018) and ablation season (30 June 2018), we used the spatial mean HS (solid curve in Figure 8).

Table 4. Performance measures ~~are shown~~ for ~~modelled $fSCA$ and the three grid cells with~~ (I) modelled $fSCA$ using JIM$_{\mathrm{OSHD}}$ and camera-retrieved $fSCA$ for the winter seasons 2016 to ~~2019 and for winter season 2018 with~~ 2020, (II) modelled $fSCA$ using JIM$_{\mathrm{OSHD}}$ and Sentinel-derived $fSCA$ ~~. Performance measured are shown~~ for ~~all~~ the three grid cells for the winter season 2018, (III) camera-derived $fSCA$ with Sentinel-derived $fSCA$ ~~. In~~ for the three grid cells, and (~~I~~IV to VII) ~~statistics are also shown~~ for all JIM modelled $fSCA$ versions ~~, namely the algorithm component $fSCA_{\mathrm{season}}$ as well as a $fSCA_{\mathrm{curr}}$, which uses the current σ_{HS} with current HS in Eq.~~ (~~1~~for details see Table 1)~~modelled with JIM$_{\mathrm{OSHD}}$. Given statistics are NRMSE, RMSE~~, ~~MPE~~namely for JIM$^{\mathrm{season}}_{\mathrm{OSHD}}$, ~~MAE~~JIM$^{\mathrm{curr}}_{\mathrm{OSHD}}$, ~~K-S test statistic~~ JIM$^{\mathrm{allHelbig}}_{\mathrm{OSHD}}$ and ~~NRMSE$_{\mathrm{quant}}$~~JIM$^{\mathrm{Swenson*}}_{\mathrm{OSHD}}$, with camera-derived $fSCA$.

$fSCA$	NRMSE	RMSE	MPE ~~MAE K-S NRMSE$_{\mathrm{quant}}$~~
	[%]		[%] ~~%~~
I JIM$_{\mathrm{OSHD}}$ vs camera			
	21	0.17	-7.1
~~I~~II JIM$_{\mathrm{OSHD}}$ vs ~~camera~~ Sentinel-2			
~~$fSCA$~~	~~21.6~~ 2	~~0.16~~ 0.02	~~-7.0~~ 0.8
III camera vs Sentinel-2	~~0.11~~	~~0.23~~	~~9.5~~
~~$fSCA_{\mathrm{season}}$ 23.3 0.17~~ height	~~-6.5~~ 12	0.11	~~0.23 8.9~~ 5.0
~~$fSCA_{\mathrm{curr}}$ 27.9 0.21 -8.1~~ heightIV JIM$^{\mathrm{season}}_{\mathrm{OSHD}}$ vs camera	~~0.13~~	~~0.32~~	~~18.6~~
~~II JIM$_{\mathrm{OSHD}}$ vs Sentinel-2~~	22	0.18	-6.1
~~$fSCA$~~ V JIM$^{\mathrm{curr}}_{\mathrm{OSHD}}$ vs camera	~~1.8~~	~~0.02~~	~~-0.7~~
	~~0.01~~ 26	~~0.53~~ 0.21	~~1.03~~ -9.2
~~III Sentinel-2~~ VI JIM$^{\mathrm{allHelbig}}_{\mathrm{OSHD}}$ vs camera			
	21	0.17	-7.6
~~$fSCA$~~ VII JIM$^{\mathrm{Swenson*}}_{\mathrm{OSHD}}$ vs camera	~~11.5~~	~~0.11~~	~~5.0~~
	~~0.06~~ 30	~~0.57~~ 0.25	~~6.5~~ -10.6

~~From this we estimated the end of spatial mean~~ black line at bottom of Figure 9). Overall, differences in performance between the accumulation and the ~~start of spatial mean ablation period for Switzerland at 1 April 2018 (vertical dashed black line in Figure 8). Until the start of the ablation periodwe obtain the most scatter~~ ablation period were small (I in Table 5). However, there were marked differences with elevation throughout the season. Up to the end of the accumulation period, the largest differences between modelled and Sentinel-derived $fSCA$ were at elevations lower than 1500 m, whereas at ~~higher elevations both~~ elevations above around 3000 m the agreement was good (Figure 9a). During the ablation period, most of the snow at lower elevations was gone, and modelled $fSCA$ ~~agree well. At 30 June about 15 % of the seasonal maximum spatial mean HS is left which concentrates at high elevations above about 2700 m (vertical line with stars in Figure 8). From~~ was generally larger than Sentinel-derived $fSCA$ at higher elevations (> 2500 m), in particular towards the end of the ablation season. During the summer (30 June ~~2018 until~~ to 30 August 2018), i.e. ~~during summer~~after the end of the ablation season, modelled $fSCA$

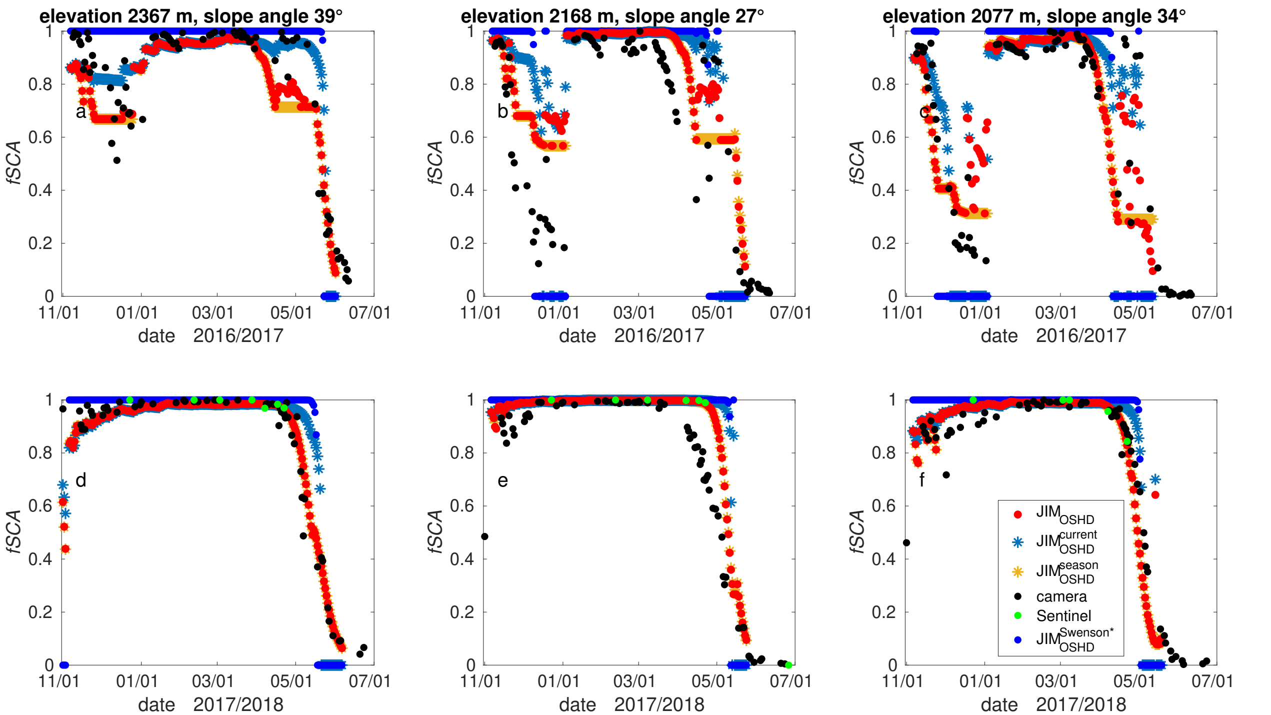

Figure 8. Modelled $fSCA$, $fSCA_{\text{season}}$, $fSCA_{\text{curr}}$ as well as camera-derived $fSCA$ camera- and Sentinel-derived $fSCA$ for the three 1 km grid cells seen by within the field of view of the camera in Davos for two seasons: upper panel (a), (b) and (to c) winter 2017, lower panel (c), (d) and (eto f) winter 2018.
. Note that, only for illustration, we here also show camera- and Sentinel-derived $fSCA$ (black and green dots) for grid cells with modelled $HS < 5$ cm.

overestimates was larger than Sentinel-derived $fSCA$ at the highest elevations above about ($>$ 3500 mwhereas between) whereas between the snow line and these highest elevations, modelled $fSCA$ underestimates Sentinel-derived $fSCA$. For the winter season lasting from 20 December to 30 June 2018 in Switzerland we obtain a NRMSE of 20 % and a MPE of 2 % (Table 4)was generally lower.

Given the also rather high temporal resolution of the Sentinel-derived $fSCA$ data set, we again computed evaluated the $fSCA$ model simplifications , $fSCA_{\text{season}}$ and $fSCA_{\text{curr}}$. Overall errors with algorithm simplifications and $\text{JIM}_{\text{OSHD}}^{\text{Swenson*}}$ (cf. Table 1). Compared to our seasonal implementation, the overall performance values of the $fSCA$ algorithm simplifications were similar, except for $\text{JIM}_{\text{OSHD}}^{\text{curr}}$ and $\text{JIM}_{\text{OSHD}}^{\text{Swenson*}}$ (Table 5). Modelled $fSCA$ values with $\text{JIM}_{\text{OSHD}}^{\text{curr}}$ and $\text{JIM}_{\text{OSHD}}^{\text{Swenson*}}$ were generally larger than Sentinel-derived $fSCA$are only slightly worse than for modelled , resulting in larger MPE values with the largest ones for $\text{JIM}_{\text{OSHD}}^{\text{Swenson*}}$ (compare I, III and V in Table 5). This is also clearly reflected in the elevation-dependent differences between $fSCA$ using the full using $\text{JIM}_{\text{OSHD}}^{\text{Swenson*}}$ and Sentinel-derived $fSCA$ algorithm. We obtain a NRMSE of 20 % for $fSCA_{\text{season}}$ and a NRMSE of 22 % for $fSCA_{\text{curr}}$ (Table 4).

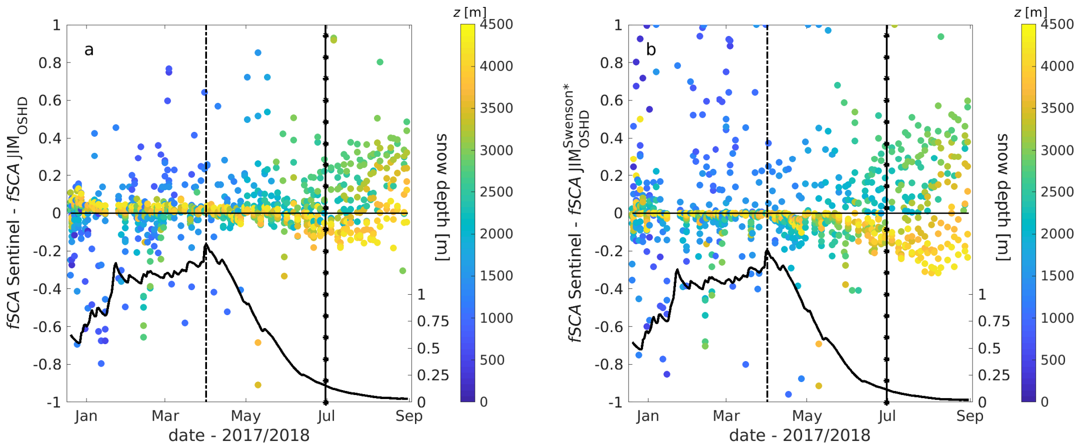

Figure 9. Difference between Sentinel-derived $fSCA$ minus and modelled $fSCA$ for Switzerland as a function of date and elevation z (in 250 m elevation bins) for available satellite dates for (a) JIM_{OSHD} and (b) $\text{JIM}^{\text{Swenson*}}_{\text{OSHD}}$. Daily spatial mean snow depth HS is also shown by the (solid black linebelow). Approximate end of accumulation and start of ablation season is indicated by the dashed The vertical line whereas lines indicate the dates for the approximate end of accumulation (dashed) and ablation season is indicated by the vertical (line with stars) season.

throughout the season (Figure 9b).

5 Discussion

5.1 Fractional snow-covered area $fSCA$ algorithm

We developed a Our seasonal $fSCA$ algorithm by combining a PoW σ_{HS} parameterization for mountainous terrain is based on the closed-form $fSCA$ parameterization of Helbig et al. (2015a) (Eq. (2)) and one for flat terrain (Eq. (3)) with tracking snow values for alternating accumulation and melt eventsthroughout the season in a closed form $fSCA$ parameterization (Eq. (1). Such an implementation of a seasonal $fSCA$ algorithm has, to the best of our knowledge, not been presented in detail so far.1) and combines two statistical parameterizations for σ_{HS} together with a tracking method to account for changes in maximum snow depth and precipitation events. The algorithm is easy to apply and only requires storing snow history and subgrid is modular, meaning that individual parts can easily be complemented or replaced with new parameterizations e.g. for $fSCA_{\text{nsnow}}$. Overall, our algorithm only requires subgrid cell summer terrain parameters, which are the a slope related parameter μ and the terrain correlation length(Section 2.2). , and tracking snow information.

At the moment we use the $\sigma^{\text{flat}}_{HS}$ parameterization We evaluated the performance of our seasonal $fSCA$ implementation in Switzerland. We could not explicitly evaluate the performance for completely flat grid cells, i.e. grid cells with a subgrid mean slope angle of zero. After removing rivers/lakes, we only had five 1 km grid cells for Switzerland with a subgrid mean slope

Table 5. Performance measures ~~between Sentinel-derived~~ for (I) modelled $fSCA$ using JIM$_{\mathrm{OSHD}}$ and ~~modelled~~ Sentinel-retrieved $fSCA$ for the winter seasons 2018 for all valid 1 km grid cells of Switzerland ~~between~~ and for all dates (20 December 2017 to 30 June 2018), for the accumulation period (20 December to 1 April) and for the ablation period (1 April to 30 June~~2018. Given statistics are NRMSE~~), ~~RMSE~~and (II to V) for all JIM modelled $fSCA$ versions (for details see Table 1), ~~MPE~~namely for JIM$_{\mathrm{OSHD}}$, ~~MAE~~JIM$^{\mathrm{season}}_{\mathrm{OSHD}}$, ~~K-S test statistic~~ JIM$^{\mathrm{curr}}_{\mathrm{OSHD}}$, JIM$^{\mathrm{allHelbig}}_{\mathrm{OSHD}}$ and ~~NRMSE$_{\mathrm{quant}}$~~JIM$^{\mathrm{Swenson*}}_{\mathrm{OSHD}}$.

$fSCA$ vs Sentinel-2	NRMSE	RMSE	MPE ~~MAE K-S NRMSE$_{\mathrm{quant}}$~~
	[%]		[%]
I JIM$_{\mathrm{OSHD}}$			
all dates	~~%~~12	0.11	0.4
accumulation period	11	0.11	0.3
ablation period	14	0.12	0.5
II JIM$^{\mathrm{season}}_{\mathrm{OSHD}}$			
all dates	12	0.12	0.4
accumulation period	11	0.11	0.3
ablation period	14	0.12	0.5
~~$fSCA$~~ III JIM$^{\mathrm{curr}}_{\mathrm{OSHD}}$	~~19.9~~	~~0.15~~	
all dates	~~1.9~~ 14	~~0.05~~ 0.13	~~0.39~~ -0.8
accumulation period	~~2.5~~11	0.11	0.1
~~$fSCA_{\mathrm{season}}$~~ ablation period	~~20.1~~ 18	~~0.15~~ 0.16	~~1.9~~ -2.4
IV JIM$^{\mathrm{allHelbig}}_{\mathrm{OSHD}}$	~~0.05~~	~~0.39~~	
all dates	~~2.6~~ 12	0.11	0.3
~~$fSCA_{\mathrm{curr}}$~~ accumulation period	~~22.0~~ 11	0.11	0.2
ablation period	14	0.12	0.5
V JIM$^{\mathrm{Swenson*}}_{\mathrm{OSHD}}$			
all dates	18	0.17	-1.8
accumulation period	17	0.16	~~1.1~~ -0.7
ablation period	~~0.06~~ 21	~~0.39~~ 0.19	~~4.5~~ -3.6

angle of zero, i.e. 0.01 % of all grid cells. For these grid cells, using $\sigma_{HS}^{\text{Helbig}}$ (Eq. (3)) to describe the spatial new snow depth distribution σ_{HS} in Eq. (1)rather than the $\sigma_{HS}^{\text{topo}}$ parameterization 3) always results in a $fSCA$ of one. As a first approach, we therefore proposed to use $\sigma_{HS}^{\text{Egli}}$ (Eq. 4). Although we see no reason why our $fSCA$ algorithm could not be used in other geographic region, it remains unclear at this point if our seasonal $fSCA$ implementation can also be used in flat regions.

We used $\sigma_{HS}^{\text{Egli}}$ (Eq. (2)). Since $\sigma_{HS}^{\text{topo}}$ was empirically derived from PoW data we found that to describe the 4), which does not account for subgrid topography, to derive $fSCA_{\text{nsnow}}$. We did this to account for uniform blanketing after a snowfall, i.e. to account for possible increases in $fSCA$ after a recent snowfall. When substituting $\sigma_{dHS}^{\text{Egli}}$ by $\sigma_{dHS}^{\text{Helbig}}$ in Eq. (6) and (7) (JIM$_{\text{OSHD}}^{\text{allHelbig}}$, cf. Table 1), the overall performance was very similar (Table 4 and 5). Thus, while applying $\sigma_{dHS}^{\text{Egli}}$ might not describe the true spatial new snow depth distributions distribution in mountainous terrainwhen the ground is typically almost completely covered by snow we might need a different description. As , the formulation is simple and is therefore used here as a first approachwe therefore use the flat field parameterization even over mountainous terrain. Though at least at lower elevations and during spring neglecting topographic interactions might be justified for new snow distributions, spatial snow depth distributions before and after snowfall accumulations should be analyzed throughout the season for confirmation.

Implementing the seasonal $fSCA$ algorithm in a distributed snow cover model allowed us to evaluate the algorithmwith spatiotemporal measurement data.We are not aware of any seasonal . Based on the modular algorithm setup, different closed-form $fSCA$ implementation that has been evaluated in detail by exploiting independent HS data sets in high spatial resolution and snow products in high temporal resolution. parameterizations can be applied in our seasonal algorithm, e.g. for a flat grid cell or for $fSCA_{\text{nsnow}}$ (for some empirical examples cf. Essery and Pomeroy, 2004).

5.2 Evaluation

5.2.1 Evaluation with $fSCA$ from fine-scale HS maps

The evaluation of the seasonal $fSCA$ algorithm with $fSCA$ from fine-scale HS maps revealed overall good performances at all six points of the season with NRMSE's always being lower than 10 % (Table 2). Performances decreased from PoW, to accumulation and later ablation. showed that overall the model performed well, especially at PoW(I in Table 3). Modelled $fSCA$ using JIM$_{\text{OSHD}}^{\text{Swenson*}}$, on the other hand, generally overestimated $fSCA$ (MPE$<$ 0). This algorithm inter-comparison shows that the seasonal $fSCA$ evolution is better captured by JIM$_{\text{OSHD}}$, most likely because the JIM$_{\text{OSHD}}^{\text{Swenson*}}$ model does not sufficiently account for the high spatial variability in snow distribution in complex terrain.

During accumulation at higher elevations, modelled $fSCA$ overestimates using JIM$_{\text{OSHD}}$ overestimated ADS-derived $fSCA$, even though modelled HS underestimates measured HS across all elevations (Figure 3a and 5agreed reasonably well with the measurements (Figure 4a and 6a). This could indicate a problem of our $fSCA$ algorithm during accumulation. In this period of the season snowfall events dominate, during which, we use the flat field standard deviation of HS (Eq. (3))to characterize $fSCA$ even on inclined grid cells. Not accounting for the various topography interactions with wind, precipitation and radiation shaping the snow depth distribution in mountainous terrain during accumulationmight have led to overestimations of modelled We also used a different model configuration (JIM$_{\text{OSHD}}^{\text{allHelbig}}$ in Table 1), yet $fSCA$ values did not substantially change for the accumulation date [not shown]. Based on this we assume that both σ_{HS} parameterizations cannot sufficiently describe snow redistribution during accumulation, likely due to periods with strong winds following snowfall. The description of spatial HS distribution during accumulation thus requires further investigations, for which howeverσ_{HS} during the accumulation period thus needs to be improved. This will, however, require more than one spatial HS data set acquired during accumulationwould be neededduring accumulation.

Except for during accumulation, modelled At PoW and during the ablation season, JIM$_{\mathrm{OSHD}}$ mostly underestimated $fSCA$ rather underestimates compared to $fSCA$ from fine-scale HS maps. However, modelled $fSCA$ does not show similar strong trends when compared to Sentinel-derived $fSCA$ but agrees rather well with $fSCA$ from Sentinel-2 snow products for the three dates (Figure 4). Largest underestimations occur for ALS data at lower elevations and during ablation where low , without a clear elevation trend (Figures 4 and 5). Discrepancies between modelled and measured HSvalues of on average lower than 30 cm dominate , on the other hand, generally increased with elevation (Figure 6). We assume that the choice of a and 7). Obviously for larger snow depth, correctly modelling HS has little effect on $fSCA$, The overall underestimated modelled $fSCA$ values were likely a consequence of the HS threshold of zero m 0 m we used to decide whether or not a 2 or 5 m grid cell was snow-covered might be one reason for the underestimationsor not. In reality, due to measurement uncertainties, both small positive or negative measured HS values might have been zero too. When increasing this can still be associated with snow free areas. When arbitrarily increasing the HS threshold to $\pm$ 10 cm resulting for the ALS-data, modelled 1 km $fSCA$ from HS maps decreased considerably and in part large overestimations of modelled $fSCA$ resulted at the various points in time of the season values were rather larger than the measurements [not shown]. This is not contradictory, but emphasizes the need to accurately model HS along snow lines, where small inaccuracies in HS can have large impacts on $fSCA$. For instance, during early ablation modelled as well as measured $fSCA$ are larger in the lowest elevation bin than at higher elevations (cf. Fig. 4c). Unfortunately, we currently do not have detailed snow observations available to define robust HS threshold values which take into account the different points in time of the season as well as varying terrain slope anglesthe influence of terrain and ground cover. However, the overall good agreement between Sentinel- and ALS-derived $fSCA$ (Figure 4 and Table 2, III) provides 5 and III in Table 3) provides some confidence in the fine-scale HS data-derived $fSCA$ used here to evaluate modelled $fSCA$.

$fSCA$ performances mostly improve with elevation or remain similar, except for during accumulation (Figure 3b,c and 4). On the contrary, performances for modelled HS mostly decrease with elevation for the same points in time (Figure 5b,c and 6). Large underestimations in modelled HS at high elevations affected modelled $fSCA$ much less than weak overestimations of measured HS at lower elevation during ablation. This is not contradictory but emphasizes the need of accurately modelled HS along snow lines where small inaccuracies in HS can have large impacts. In addition, along the snow line the valid data percentage per bin was very low with values between 1 to 5 % for all $fSCA$ from fine-scale HS data sets. Thus, a single outlier along the snow line could have also degraded the performance (e.g. Figure 5c). Note that the overall tendency of modelled HS to underestimate measured HS at high altitudes may also originate from precipitation underestimation. As there are fewer AWS at high elevations data assimilation cannot correct for any flawed precipitation input.

The two benchmark $fSCA$ models ($fSCA^{\text{measured}}_{\text{curr}}$ and $fSCA^{\text{measured}}_{\text{PoW}}$based on Eq. (1) using measured HS compare better to $fSCA$ derived from rather than modelled HS data than ($fSCA^{\text{measured}}_{\text{curr}}$ and $fSCA^{\text{measured}}_{\text{PoW}}$) generally showed similar trends as HS-derived and modelled $fSCA$ using JIM$_{\text{OSHD}}$. This result confirms the previously derived functional $tanh$-form (Eq. (1))for $fSCA$ at PoW for a seasonal application. While at the date of early ablation of ALS data, modelled (Figure 4 and 5). At PoW, $fSCA^{\text{measured}}_{\text{curr}}$ agreed less well with measured $fSCA$ performed better, this might be due to snowfalls after the date at approximate PoWwith consecutive melt (than our seasonal implementation (cf. Figure 4b and 5a). This may have altered the actual PoW snow depth distribution compared to the ALS-measured σ_{HS} at approximate date of PoW. Except for the lowest elevation bin, performances among both benchmark models are quite similar. While we would have expected at least a better performance of $fSCA^{\text{measured}}_{\text{PoW}}$ during ablation, $fSCA^{\text{measured}}_{\text{curr}}$ performs slightly better during early ablation. The reason for this is most likely the same than why modelled indicate uncertainties in the empirical $fSCA$ outperformed both benchmark models at that early ablation date (Figure 4parameterization (Eq. 1), which requires further investigation of spatial HS data sets during accumulation. During ablation, we expected that $fSCA^{\text{measured}}_{\text{PoW}}$ would be closer to measured $fSCA$ than $fSCA^{\text{measured}}_{\text{curr}}$, which was however not the case (cf. Figure 4c and 5b). Due to snowfalls after the approximate date of PoW of ALS data, at some elevations, the actual PoWsnow depth distribution does not agree with the one at approximate date of PoW of ALS data at these elevations anymore. Applying a snow cover model that tracks the history of HS to derive seasonal $fSCA$ is thus beneficial. Evaluating the benchmark $fSCA$ models with Since the true PoW date is elevation and aspect dependent, we cannot assume that one date for PoW is representative for the entire catchment, covering several hundred of square kilometers and large elevation gradients. Thus, measured σ_{HS} at the date we defined as PoW, might not have been representative for the true $\sigma_{HS_{\text{max}}}$ in each grid cell as required by Eq. (5). Besides possible uncertainties in the empirical $fSCA$ derived from parameterization (Eq. 1), we assume this is the main reason why these two benchmark models using measured HS data confirmed the overall applicability of did not outperform our seasonal implementation. Overall, these comparisons emphasize the need for tracking snow information per grid cell, as is done by our seasonal $fSCA$ algorithm.

5.2.2 Evaluation with camera-derived $fSCA$

While the evaluation of the seasonal $fSCA$ algorithm with $fSCA$ from The evaluation with fine-scale HS maps revealed overall good performances model performance at six points in time, seasonal performances could not be evaluated continuously . It was however not possible to comprehensively evaluate the performance over the season. Evaluating with For this, we used daily camera-derived $fSCA$demonstrated that modelled , showing that the modelled seasonal $fSCA$ was able to mostly reproduce well the seasonal trend (Figure 7trend was mostly in line with observations (Figure 8).

However, overall, modelled $fSCA$ compared less well to Model performance compared to the camera-derived $fSCA$ than modelled $fSCA$ compared values was overall worse than when comparing to HS-derived $fSCA$ (e.g. NRMSE of 22 % 21 % for I in Table 4 compared to NRMSE to 9 % ; Table 2, I versus Table 2 , I) . These overall larger errors most likely originate in an of 7 % for I in Table 3). Since the higher temporal resolution of the camera data set leads to the largest spread in $fSCA$ values compared to the other two data sets (cf. Table 2 and Fig. 3), a larger portion of intermediate $fSCA$ values (e.g. close to the snow line) are included which are generally more difficult to model correctly than $fSCA$ values close to one. The poorer model performance is however likely also be due to the overall lower accuracy of camera-derived $fSCA$compared to $fSCA$ from fine-scale HS maps. For instance, the projection of the 2D-camera image to a 3D DEM may introduce errors and distortions. Furthermore, when deriving $fSCA$ from camera images, clouds/fog and uneven illuminationdue to for instance , for instance due to shading or partial cloud covermay compromise the possibility of detecting snow by the snow classification algorithm of Salvatori et al. (2011) and can , may deteriorate the accuracy (e.g. Farinotti et al., 2010; Fedorov et al., 2016; Härer et al., 2016; Portenier et al., 2020). The choice of the threshold method when automatically deriving $fSCA$ from the images also introduces uncertainty. Here, we decided that the method proposed by Salvatori et al. (2011) followed the seasonal modelled $fSCA$ trend best though some uncertainty remained. For instance, the decreased performances by about 10 % of the NRMSE in season 2019 and 2020 could stem from an increase in Another factor affecting the performance measures was the threshold for the number of image pixels when the camera was upgraded. This may have led to more detailed information when e.g. small vegetation is resolved. The overall better agreement between modelled and Sentinel-derived $fSCA$ than between between Sentinel- and camera-derived $fSCA$ (NRMSE of 2 % versus 12 %, cf. Table 2) similarly indicates some larger uncertainties in the camera-derived valid fine-scale data per 1 km grid cell. When aggregating to 1 km $fSCA$ data set. For instance, while maps for the Sentinel-derived values, we required at least 50 % valid fine-scale information for the Sentinel-derived $fSCA$ when aggregating to 1 km $fSCA$ maps, this data. This requirement could not be met for camera-derived $fSCA$. For the three 1 km model grid cells , as the projected fractions of the camera FOV are on the 1 km model grid cells were only 9 %, 13 % and 14 %, which is much lower than the 50 % but is also used to evaluate modelled $fSCA$ for the full grid cell area. On the other hand, while it seems that there is a . This is reflected in the better agreement between modelled and Sentinel-derived and modelled $fSCA$ than between camera-derived and modelled camera- and Sentinel-derived $fSCA$, (NRMSE of 2 % versus 12 % in Table 4). Finally, as the camera was installed at valley bottom, steep slope sections cover larger areas of the FOV, while flatter slope parts remain invisible. This likely lead to underestimated $fSCA$ values. On the other hand, valid Sentinel-derived $fCSA$ $fSCA$ has a much lower temporal resolution and did not cover the entire ablation period. Instead, Sentinel-derived $fSCA$ was often available throughout the period when $fSCA$ was rather close to one (cf. Figure 78d,e). Thus, while there is likely more uncertainty in camera-derived $fSCA$, the snow cover model might have also underestimated snow melt which led to overestimated modelled HS and thus $fSCA$ at the beginning of ablation (cf. Figure 7e).

The high temporal resolution of this product still provides valuable information on model performance throughout the season.

We used the camera-derived $fSCA$ allowed us to evaluate modelled simplifications of the to also evaluate simplifications of our seasonal $fSCA$ algorithm , i.e. $fSCA_{season}$ and $fSCA_{curr}$ (JIM^{season}_{OSHD} and JIM^{curr}_{OSHD}). While the overall performance decrease is rather low with for instance an increase in NRMSE by 1 % for JIM^{season}_{OSHD} and by 6 % for JIM^{curr}_{OSHD} compared to the full $fSCA$ model, seasonal performance trends are clearly poorer than when applying the full $fSCA$ model (Figure 7). The reason that this deterioration is not seen in the overall error measures is most likely due to less frequent camera-derived $fSCA$ at time steps during or following snowfall events when clouds or bad illumination might have prevented deriving valid $fSCA$ from images. While the in part large overestimations of camera-derived as well as $JIM^{Swenson*}_{OSHD}$ (Table 1). Compared to our seasonal $fSCA$ increase from JIM^{season}_{OSHD} to implementation, the more simple implementations did not capture the seasonal variation as well (Figure 8). With JIM$^{curr}_{OSHD}$, ~~with JIM$^{curr}_{OSHD}$~~ the start of the ablation season ~~is not only delayedbut~~ was delayed, and the ablation season ~~is~~ was also considerably shortened, by up to ~~46~~ 21 days. In ~~principle, $fSCA_{curr}$ describes seasonal~~ this respect, the results for JIM$^{Swenson*}_{OSHD}$ were very similar, as overall the increases and decreases of $fSCA$ ~~as if staying continuously at peak winter, though for various HS values. However, this leads to sudden jumps when current HS approaches zero, as seen by the steep melt outs of~~ were very steep, leading to shortened snow seasons and poorer performances (cf. Table 4). In principle, JIM$^{curr}_{OSHD}$ ~~, or when current~~ considers each day as PoW, leading to rapid changes in $fSCA$, in particular when HS ~~raises from no snow to a value larger than zero following snowfall events on bare ground, as seen during accumulation for JIM$^{curr}_{OSHD}$. Thus, while including the tracking of current seasonal maximum~~ values are low (i.e. early accumulation or ablation season). In JIM$^{season}_{OSHD}$, the seasonal maximum value of HS ~~to derive the current maximum σ_{HS} already improved the seasonal trends ($fSCA_{season}$), additional accounting for $fSCA_{nsnow}$ is able to overcome the remaining differences between $fSCA_{season}$ and modelled~~ was additionally tracked, substantially improving the seasonal $fSCA$ ~~derived by the full~~ trend, in particular during the ablation season. However, changes in $fSCA$ ~~algorithm~~due to snowfall events were still not captured well with this implementation, showing that our new snow tracking algorithm further improves the overall model performance. Since the impact of using JIM$^{allHelbig}_{OSHD}$ on modelled $fSCA$ is mainly restricted to snowfall following melt periods, overall performances were very similar to JIM$_{OSHD}$ (cf. Table 4 and 5). This again indicates that the description of σ_{HS} following snowfall events requires further investigation.

5.2.3 Evaluation with Sentinel-derived $fSCA$

By including Sentinel-derived $fSCA$ in our evaluation~~data set to evaluate modelled $fSCA$~~, we added a data set ~~that unites a rather high temporal data resolution with~~ with both a high temporal resolution and a much larger spatial coverage ~~than was inherent in the two other evaluation data sets~~ (cf. Table ~~1~~2). The Sentinel-derived $fSCA$ data set ~~comprises about 275~~comprised about 217'000 1 km grid cells covering a wide range in terrain elevations, slope angles and terrain aspects. ~~This variety was not achieved for the high-temporal evaluation with camera-derived $fSCA$ limited to one southeast-facing slope with overall similar elevations between 2077 m and 2367 m and slope angles between 27 and 39 (cf. Figure 2b).~~

For the ~~one winter seasoninvestigated, we obtained~~ investigated winter season, results showed an overall good seasonal agreement across Switzerland, though there was some elevation-dependent scatter ~~exists (Figure 8). The majority of the largest scatter occurs during the accumulation period~~ (Figure 9a). Discrepancies during accumulation occurred mostly along the snowline at lower elevations, where lower spatial HS values as well as more cloudy weather prevail during accumulation. ~~By neglecting all 1 km domains with modelled HS lower than 5 cm, which would also resemble the preprocessing of fine-scale HS-derived $fSCA$ (cf. Section 3.3), the scatter between modelled~~ Both can lead to inaccurate modelled and Sentinel-derived $fSCA$. Furthermore, we assume that some of the overestimations in modelled $fSCA$ at ~~these lower~~ higher elevations during accumulation ~~reduced considerably and the overall performances improved substantially. For instance the NRMSE reduced from 20 % to 12 % and the MPE from 1.9 % to 0.23 %.~~ could also stem from underestimated σ_{HS} during periods when strong winds follow snowfall events, as was also observed in the HS data sets (Figure 4a and Section 5.2.1). The scatter at ~~higher elevations during summer might originate from underestimated~~ high elevations during ablation and summer likely originates from lower modelled $fSCA$ due to underestimated precipitation~~(~~, as there are fewer AWS at high elevations ~~).~~ for data assimilation in our model.

~~Similar than for camera-derived $fSCA$ the overall performance decrease when using $\mathrm{JIM}^{\mathrm{season}}_{\mathrm{OSHD}}$ and $\mathrm{JIM}^{\mathrm{curr}}_{\mathrm{OSHD}}$ is rather low with for instance an increase in NRMSE by 0.2 % for $\mathrm{JIM}^{\mathrm{season}}_{\mathrm{OSHD}}$ and by 2 % for $\mathrm{JIM}^{\mathrm{curr}}_{\mathrm{OSHD}}$ compared to the full $fSCA$ model. When binned per elevation for Switzerland a small increase in scatter only appeared between modelled $fSCA$ and $fSCA_{\mathrm{curr}}$ towards the end of the season not shown. While we in part obtained large differences for individual grid cells between the three modelled $fSCA$ and camera-derived $fSCA$, performances between modelled and Sentinel-derived $fSCA$ only improved slightly compared to when applying $\mathrm{JIM}^{\mathrm{season}}_{\mathrm{OSHD}}$ or $\mathrm{JIM}^{\mathrm{curr}}_{\mathrm{OSHD}}$ over a much larger spatial coverage. We assume that the lack of a stronger improvement in the overall error measures is due to more missing valid satellite coverage during clouded periods that typically occur during or after snowfalls. Yet exactly during these periods we would expect larger differences due to the missing new snow $fSCA$ updates when e.g. reducing the full $fSCA$ model to $fSCA^{\mathrm{season}}$ (cf. Figure 7b,c). Overall, we obtained poorer performance measures between modelled $fSCA$ and Sentinel- as well as camera-derived $fSCA$ compared to between modelled $fSCA$ and $fSCA$~~ Performance measures were somewhat poorer as those from fine-scale HS maps (e.g. ~~a NRMSE of 20 % for Sentinel-2 $fSCA$, of 22 % for camera $fSCA$ and of 9 % for~~ NRMSE of 12 % for Sentinel versus 7 % for $fSCA$ ~~from~~ for HS data). Uncertainties introduced by reduced visibility in the snow products of Sentinel-2 ~~and the camera are most likely the reason~~ are the most likely reason for this. Both, our camera- as well as the Sentinel-2 data set cover long time periods in higher temporal resolution, i.e. they include also periods under unfavorable weather conditions. On the contrary, clear sky dates were carefully selected for the on-demand high-quality data acquisitions from the air for our $fSCA$ data sets derived from fine-scale HS maps. Nevertheless, the camera- as well as the Sentinel-2 data set enabled us to evaluate seasonal $fSCA$ model trends which would not have been possible ~~alone from the~~ from only six $fSCA$ data sets derived from HS data.

When evaluating the simplified $fSCA$ algorithms and $\mathrm{JIM}^{\mathrm{Swenson*}}_{\mathrm{OSHD}}$, model performance measures were comparable to our seasonal implementation except for $\mathrm{JIM}^{\mathrm{curr}}_{\mathrm{OSHD}}$ and $\mathrm{JIM}^{\mathrm{Swenson*}}_{\mathrm{OSHD}}$ (Table 5), as was also the case for the comparison with camera-derived $fSCA$ (Table 4). For Sentinel- and camera-derived $fSCA$, the main reason is likely the limited availability of $fSCA$ data during or shortly after snowfall, due to bad visibility and clouds. Additionally, for the Sentinel-derived $fSCA$, local performance differences across Switzerland are likely averaged out. Nevertheless, $fSCA$ values when using $\mathrm{JIM}^{\mathrm{Swenson*}}_{\mathrm{OSHD}}$ were overestimated compared to Sentinel-derived values (Figure 9b, and negative MPE for V in Table 5). Similar results were also observed when using $\mathrm{JIM}^{\mathrm{curr}}_{\mathrm{OSHD}}$ (cf. negative MPE for III in Table 5). These biases are most likely related to the rather steep increases and decreases of modelled $fSCA$ over the season, as we also observed with the camera-derived $fSCA$ (Figure 8). We further assume that overestimated $fSCA$ using $\mathrm{JIM}^{\mathrm{Swenson*}}_{\mathrm{OSHD}}$ at higher elevations, due to underestimating spatial snow depth variability in complex terrain, may have compensated for other modelled $fSCA$ error sources (e.g. from underestimated precipitation input at these elevations) leading to an overall lower bias at higher elevations during accumulation compared to our $fSCA$ implementation. Finally, note that the scatter above zero between Sentinel-derived and $\mathrm{JIM}^{\mathrm{Swenson*}}_{\mathrm{OSHD}}$ $fSCA$ (Figure 9b) almost disappears when we neglect all 1 km domains with modelled $HS < 5$ cm using $\mathrm{JIM}^{\mathrm{Swenson*}}_{\mathrm{OSHD}}$ [not shown]. While the overall NRMSE values for $\mathrm{JIM}^{\mathrm{Swenson*}}_{\mathrm{OSHD}}$ are then comparable to our seasonal implementation (e.g. NRMSE of 12 % for all dates instead of 18 %; cf. V in Table 5), it reveals the overall overestimation of JIM$_{\mathrm{OSHD}}^{\mathrm{Swenson*}}$ (e.g. increased negative MPE of -4.1 % for all dates instead of -1.8 %). Clearly, our seasonal $fSCA$ implementation is better suited to more realistically represent seasonal changes in mountainous terrain, in particular following snowfall and during the ablation period.

6 Conclusions

We presented a seasonal fractional snow-covered area ($fSCA$) algorithm based on the $fSCA$ parameterization of Helbig et al. (2015b, 2021). The seasonal algorithm is based on tracking HS and SWE values accounting for alternating snow accumulation and melt events. Two empirical parameterizations ~~are applied~~ were used to describe the spatial snow depth distribution, one for mountainous terrain ~~at PoW and one for flat terrain during a snowfall~~and one not accounting for subgrid topography. An implementation in a multilayer energy balance snow cover model system (JIM$_{\mathrm{OSHD}}$; JIM, JULES investigation model (Essery et al., 2013)) allowed us to evaluate seasonally modelled $fSCA$ for Switzerland.

Compiling independent $fSCA$ data sets with different spatiotemporal characteristics enabled a thorough ~~spatiotemporal~~ analysis of the seasonal $fSCA$ algorithm in mountainous terrain of daily 1km-$fSCA$ values. While the evaluation with the three data sets showed overall good seasonal performance, each of the evaluation data sets allowed ~~to draw additional~~ drawing specific conclusions. The evaluation with fine-scale spatial HS-derived $fSCA$ showed that ~~snow depth~~ HS uncertainties along the snow line likely contributed ~~to the largest~~ most to underestimation of $fSCA$ ~~underestimations during ablation compared to the overall best agreement at PoW~~during ablation and PoW, emphasizing the need to accurately model HS along snow lines. The camera-derived $fSCA$ data set, with the highest temporal resolution ~~,~~ confirmed the need for tracking HS over the season as well as accounting for intermediate snowfalls to avoid a delayed melt start and a ~~drastically~~ drastic shortening of the ablation season. The Sentinel-derived $fSCA$ data set, with the largest spatial coverage together with a rather high temporal resolution, demonstrated that the seasonal $fSCA$ algorithm performs well across a range of elevations, slope angles, terrain aspects and snow regimes. This comparison showed that there were some differences at low elevation ~~coinciding with very~~ or along the snowline coinciding with low HS~~early in the season~~, while discrepancies ~~occured~~ occurred mostly at high elevations towards the end of the season, respectively during summer.

Overall, NRMSE's for seasonally modelled $fSCA$ increased from ~~9~~ 7 % for HS data-derived $fSCA$, to ~~20~~ 12 % for Sentinel-derived $fSCA$ and to ~~22~~ 21 % for camera-derived $fSCA$. While the large ~~margin~~ variation in performance measures is likely tied to the various temporal and spatial resolutions of the data sets ~~leading to different data~~ and measurement uncertainties, it also demonstrates the difficulties in drawing conclusions when evaluating a model algorithm with evaluation data from different acquisition platforms. Nevertheless, this comparison with data covering a wide range of spatiotemporal scales allowed us to obtain a comprehensive overview of the strength and weaknesses of our seasonal $fSCA$ implementation. We are not aware of any seasonal $fSCA$ implementation that has been evaluated in such detail by exploiting independent HS and snow product data sets in high spatial and temporal resolution.

By implementing the $fSCA$ parameterizations applied in CLM5.0 (Lawrence et al., 2018) in JIM$_{\mathrm{OSHD}}$, we also evaluated modelled $fSCA$ using JIM$_{\mathrm{OSHD}}^{\mathrm{Swenson*}}$. This showed that our seasonal $fSCA$ algorithm captures the seasonal variation best, and that seasonal variation in $\mathrm{JIM}^{\mathrm{Swenson*}}_{\mathrm{OSHD}}$ was limited. $\mathrm{JIM}^{\mathrm{Swenson*}}_{\mathrm{OSHD}}$ resulted in often overestimated $fSCA$ values, likely because the high spatial variability in snow depth distribution in complex terrain is not sufficiently described.

The implementation of the seasonal $fSCA$ algorithm in a model only requires tracking HS and SWE for a coarse grid cell as well as deriving subgrid summer subgrid terrain parameters from a fine-scale summer DEM in combination with tracking HS and SWE for coarse grid cells. The algorithm is set up such that improvements or adaptations of individual algorithm parts can easily be implemented. The PoW $fSCA$ parameterization of Helbig et al. (2021) Helbig et al. (2015b) forms the centerpiece of the presented seasonal $fSCA$ algorithm. The recent evaluation re-evaluation with various spatial PoW snow depth data sets from 7 geographic regions showed an overall NRMSE of only 2 % (Helbig et al., 2021). This detailed evaluation at PoW in different geographic regions and the seasonal evaluation together with the seasonal assessment with the three $fSCA$ data pools presented here, suggests that the seasonal $fSCA$ algorithm may perform similar in most also be used in other geographic regions. However, further investigations, once more spatial HS data sets before and after snowfalls in complex topography become available, would be advantageous for improvements of our seasonal $fSCA$ algorithmduring a snowfall, especially during the accumulation period.

Code availability. The code of the full algorithm is made available on WSL/SLF GitLab repository as well as on Envidat upon final publication.

Data availability. All data used in this study is described in the data section. The data can be downloaded from the referenced repositories or data availability is described in the referenced publications. Theia snow maps are freely distributed via the Theia portal (https://doi.org/10.24400/329360/F7Q52MNK).

Competing interests. The authors declare that they have no conflict of interest.

Acknowledgements. We thank Andreas Stoffel at SLF for his help with GIS processing of the satellite images. N. Helbig was funded by a grant of the Swiss National Science Foundation (SNF) (Grant N° IZSEZ_186887), as well as partly funded by the Federal Office of the Environment FOEN.

6.1 Appendix: Technical aspects - Seasonal $fSCA$ implementation

The technical aspects of the different $fSCA$ (cf. box in the middle of in Figure 1), i.e. the seasonal $fSCA$ ($fSCA_{\mathrm{season}}$) and the $fSCA$ for snowfall events ($fSCA_{\mathrm{nsnow}}$), are given here. This description gives the necessary details to implement the seasonal $fSCA$ algorithm in a snow cover model. We first present some pseudocode and then give a detailed text description. !! *Seasonal $fSCA$ algorithm*1 **for** each grid cell do 2 !! *Update SWE history (buffer) from past 14* *days with current SWE*3 SWE_{buffer}(current)=SWE4 !! *Calculate max, min and recent min indices in 14 days SWE_{buffer}*5 $\mathrm{max}_{\mathrm{buff}}$, $\mathrm{min}_{\mathrm{buff}}$, $\mathrm{recentmin}_{\mathrm{buff}}$6 !! *Apply indices to finding new snow depth changes ΔHS*7 !! *New snow amount in 14 days buffer* 8 14 day ΔHS = HS - $HS(\mathrm{min}_{\mathrm{buff}})$9 !! *Recent new snow amount in 14 days buffer*10 recent ΔHS = HS - $HS(\mathrm{recentmin}_{\mathrm{buff}})$11 !! *Max snow depth change in 14 days buffer*12 max ΔHS = $HS(\mathrm{max}_{\mathrm{buff}})$ - $HS(\mathrm{min}_{\mathrm{buff}})$13 !! *Find current absolute max and pseudo-min SWE values*14 IF SWE is zero, set SWE_{max} and $SWE_{\mathrm{pseudo\text{-}min}}$ to zero15 IF $SWE \geq SWE_{\mathrm{max}}$, set SWE_{max} and $SWE_{\mathrm{pseudo\text{-}min}}$ to SWE16 IF $SWE < SWE_{\mathrm{max}}$ and $SWE < SWE_{\mathrm{pseudo\text{-}min}}$, set $SWE_{\mathrm{pseudo\text{-}min}} = SWE$17 set HS_{max}, $HS_{\mathrm{pseudo\text{-}min}}$ according to SWE_{max},$SWE_{\mathrm{pseudo\text{-}min}}$18 !! *Start calculating $fSCA$*19 !! *$fSCA_{season}$ using Eq. (1)-(3)* 20 IF grid cell is flat21 $\sigma_{HS\mathrm{season}}$:= Eq. (3) with HS_{max}22 ELSE 23 $\sigma_{HS\mathrm{season}}$:= Eq. (2) with HS_{max}24 $fSCA_{\mathrm{season}}$:= Eq. (1) with $\sigma_{HS\mathrm{season}}$ and $HS_{\mathrm{pseudo\text{-}min}}$25 !! *$fSCA_{14daynsnow}$ using Eq. (1) and (3)*26 $\sigma_{HS\mathrm{14d}}$:= Eq. (3) with max ΔHS27 $fSCA_{\mathrm{14daynsnow}}$:= Eq. (1) with $\sigma_{HS\mathrm{14d}}$ and 14 day ΔHS28 !! *$fSCA_{recentnsnow}$ using Eq. (1) and (3)*29 $\sigma_{HS\mathrm{recent}}$:= Eq. (3) with recent ΔHS30 $fSCA_{\mathrm{recentnsnow}}$:= Eq. (1) with $\sigma_{HS\mathrm{recent}}$ and recent ΔHS31 !! *Deriving $fSCA_{nsnow}$*32 $fSCA_{\mathrm{nsnow}}$ =max($fSCA_{\mathrm{14daynsnow}}$,$fSCA_{\mathrm{recentnsnow}}$)33 !! *Reset $fSCA_{season}$, if new snow is really melting*34 IF $fSCA_{\mathrm{nsnow}} > 0$ and $fSCA_{\mathrm{nsnow}} < fSCA_{\mathrm{season}}$35 $SWE_{\mathrm{pseudo\text{-}min}} = SWE$ and $HS_{\mathrm{pseudo\text{-}min}} = HS$!! *Calculate coefficient of variation from seasonal values*37 $CV_{\mathrm{season}} = \sigma_{HSseason}/HS_{\mathrm{max}}$ 38 !! *Recalculate current absolute HS_{max}*39 $HS_{\mathrm{max}} = 1.3 HS_{\mathrm{pseudo\text{-}min}}/(CV_{\mathrm{season}}\mathrm{atanh}(fSCA_{\mathrm{season}}))$ 40 !! *Recalculate current absolute SWE_{max}*41 $SWE_{\mathrm{max}} = \rho_{\mathrm{max}} HS_{\mathrm{max}}$ 42 !! *Recalculate $fSCA_{season}$*43 IF grid cell is flat44 $\sigma_{HS\mathrm{season}}$:= Eq. (3) with HS_{max}45 ELSE 46 $\sigma_{HS\mathrm{season}}$:= Eq. (2) with HS_{max}47 $fSCA_{\mathrm{season}}$:= Eq. (1) with $\sigma_{HS\mathrm{season}}$ and $HS_{\mathrm{pseudo\text{-}min}}$48 $fSCA_{\mathrm{nsnow}}$:=049 !! *Calculate final $fSCA$*50 $fSCA$=max($fSCA_{\mathrm{season}}$,$fSCA_{\mathrm{nsnow}}$)

Following new snow accumulation, the ground is almost completely covered by snow, which may lead to a different spatial snow depth variability than at PoW. We account for this by using $\sigma_{HS}^{\mathrm{flat}}$ rather than $\sigma_{HS}^{\mathrm{topo}}$ for the derivation of $fSCA_{\mathrm{nsnow}}$ to avoid introducing topography interactions in new snow σ_{HS} which were derived for PoW σ_{HS}. To calculate $fSCA_{\mathrm{nsnow}}$ we insert new snow amounts in Eq. (1)-(3). Thus, $fSCA_{\mathrm{nsnow}}$ describes the contribution to $fSCA$ solely from the new snow, i.e. as if the new snow fell on bare ground. Two $fSCA_{\mathrm{nsnow}}$ are derived: $fSCA_{\mathrm{14daynsnow}}$ for a new snow event within the last 14 days and a $fSCA_{\mathrm{recentnsnow}}$ for the most recent new snow event. To calculate both, $fSCA_{\mathrm{14daynsnow}}$ and $fSCA_{\mathrm{recentnsnow}}$, we store HS of the last 14 days. For $fSCA_{\mathrm{14daynsnow}}$ we derive the absolute maximum as well as the absolute minimum from this time window. The difference between these two extreme HS values is used to compute the corresponding σ_{HS} and the difference between current and absolute minimum HS is inserted in the numerator to obtain $fSCA_{\mathrm{14daynsnow}}$ as $fSCA$. To compute $fSCA_{\mathrm{recentnsnow}}$ we determine the first local HS minimum from the 14 days time window by going back in time. The difference between current and this local minimum HS is used to derive σ_{HS} and is also used in the numerator of $fSCA_{\mathrm{recentnsnow}}$. The maximum of $fSCA_{\mathrm{14daynsnow}}$ and $fSCA_{\mathrm{recentnsnow}}$ gives us $fSCA_{\mathrm{nsnow}}$ for that time step and grid cell.

To describe the overall seasonal $fSCA$ development we use a $fSCA_{\mathrm{season}}$ which we compute with $\sigma_{HS}^{\mathrm{topo}}$. For grid cells with slope angles equal to zero we use $\sigma_{HS}^{\mathrm{flat}}$.

To compute $fSCA_{\text{season}}$ we use current seasonal maximum HS to derive $\sigma_{HS}^{\text{topo}}$ or $\sigma_{HS}^{\text{flat}}$. In the numerator of $fSCA_{\text{season}}$ we use a HS variable which we call a pseudo-minimum HS solely to differentiate it from real global and local minima. The pseudo-minimum HS is used in $fSCA_{\text{season}}$ to derive a $fSCA$ as if there was no previous snowfall. We do this to obtain two separate $fSCA$, one $fSCA_{\text{nsnow}}$ and one $fSCA_{\text{season}}$, which will be compared afterwards. During accumulation, the pseudo-minimum HS is the current HS up until a snow event starts, following a previous melt period. Then the pseudo-minimum HS keeps the pre-snow event HS value up until current HS reaches the current seasonal maximum HS again. From then on the pseudo-minimum HS is the current HS again. During ablation, the pseudo-minimum HS matches, similar as during accumulation, the current HS up until a snow event starts. Then the pseudo-minimum HS keeps the pre-snow event HS value up until current HS falls below the pre-snow HS value again or increases up to a new current seasonal maximum HS. However, once the $fSCA_{\text{nsnow}}$ is again lower than $fSCA_{\text{season}}$ and the newly fallen snow has started to melt ($SWE_{t-1} - SWE_t > 2$ mm), we recalculate the current seasonal maximum HS. Then, we update $fSCA_{\text{season}}$ using the new current seasonal maximum HS for σ_{HS} and the pseudo-minimum HS taking the current HS in the numerator. We perform the recalculation of the seasonal maximum HS to account for an increased seasonal σ_{HS} caused by the intermediate snow event. The recalculated seasonal maximum HS takes that value that allows to arrive at the current HS by melt only, i.e. without intermediate snowfall. For the recalculation procedure we solve the seasonal CV from before the snow event, i.e. σ_{HS}/HS both using the previous seasonal maximum HS, for σ_{HS} and insert it in $fSCA_{\text{season}}$. By further using the pseudo-minimum HS (which was set to the current HS) in $fSCA_{\text{season}}$ we derive a new seasonal maximum HS. At the end of this adjustment $fSCA_{\text{nsnow}}$ is set to zero and an updated (larger) seasonal maximum HS with a similar or slightly lower $fSCA_{\text{season}}$ results.

References

Andreadis, K. M. and Lettenmaier, D. P.: Assimilating remotely sensed snow observations into a macroscale hydrology model, Adv. Water Resour., 29, 872–886, 2006.

Baba, M. W., Gascoin, S., and Hanich, L.: Assimilation of Sentinel-2 Data into a Snowpack Model in the High Atlas of Morocco, Remote Sens., 10, 1982, https://doi.org/10.3390/rs10121982, 2018.

Bellaire, S. and Jamieson, B.: Forecasting the formation of critical snow layers using a coupled snow cover and weather model, Cold. Reg. Sci. Technol., 94, 37–44, 2013.

Bühler, Y., Marty, M., Egli, L., Veitinger, J., Jonas, T., Thee, P., and Ginzler, C.: Snow depth mapping in high-alpine catchments using digital photogrammetry, Cryosphere, 9, 229–243, https://doi.org/10.5194/tc-9-229-2015, 2015.

Cluzet, B., Revuelto, J., Lafaysse, M., Tuzet, F., Cosme, E., Picard, G., Arnaud, L., and Dumont, M.: Towards the assimilation of satellite reflectance into semi-distributed ensemble snowpack simulations, Cold Regions Science and Technology, 170, 102 918, https://doi.org/https://doi.org/10.1016/j.coldregions.2019.102918, 2020.

Doms, G., Förstner, J., Heise, E., Herzog, H. J., Mironov, D., Raschendorfer, M., Reinhardt, T., Ritter, B., Schrodin, R., Schulz, J. P., and Vogel, G.: A Description of the Nonhydrostatic Regional COSMO Model, Part II: Physical Parameterization, LM F90 4.20 38, Consortium for Small-Scale Modelling,Printed at Deutscher Wetterdienst,63004 Offenbach,Germany, 2011.

Douville, H., Royer, J.-F., and Mahfouf, J.-F.: A new snow parameterization for the Météo-France climate model Part II: validation in a 3-D GCM experiment, Climate Dynamics, 1, 37–52, 1995.

Drusch, M., Del Bello, U., Carlier, S., Colin, O., Fernandez, V., Gascon, F., Hoersch, B., Isola, C., Laberinti, P., Martimort, P., et al.: Sentinel-2: ESA's optical high-resolution mission for GMES operational services, Remote Sensing of Environment, 120, 25–36, 2012.

Egli, L. and Jonas, T.: Hysteretic dynamics of seasonal snow depth distribution in the Swiss Alps, Geophys. Res. Lett., 36, 2009.

Essery, R.: Large-scale simulations of snow albedo masking by forests, Geophys. Res. Lett., 40, 5521–5525, https://doi.org/10.1002/grl.51008, 2013.

Essery, R. and Pomeroy, J.: Implications of spatial distributions of snow mass and melt rate for snow-cover depletion: theoretical considerations, Ann. Glaciol., 38, 2004.

Essery, R., Morin, S., Lejeune, Y., and Ménard, C. B.: A comparison of 1701 snow models using observations from an alpine site, Adv. Water Resour., 55, 131–148, 2013.

Farinotti, D., Magnusson, J., Huss, M., and Bauder, A.: Snow accumulation distribution inferred from time-lapse photography and simple modelling, Hydrological Processes, 24, 2087–2097, https://doi.org/10.1002/hyp.7629, 2010.

Fedorov, R., Camerada, A., Fraternali, P., and Tagliasacchi, M.: Estimating Snow Cover From Publicly Available Images, IEEE Transactions on Multimedia, 18, 1187–1200, https://doi.org/10.1109/TMM.2016.2535356, 2016.

Gascoin, S., Hagolle, O., Huc, M., Jarlan, L., Dejoux, J.-F., Szczypta, C., Marti, R., and Sánchez, R.: A snow cover climatology for the Pyrenees from MODIS snow products, Hydrol. Earth Syst. Sci., 19, 2337–2351, 2015.

Gascoin, S., Grizonnet, M., Bouchet, M., Salgues, G., and Hagolle, O.: Theia Snow collection: high resolution operational snow cover maps from Sentinel-2 and Landsat-8 data, Earth Syst. Sci. Data, pp. 493–514, https://doi.org/10.5194/essd-11-493-2019, 2019.

Griessinger, N., Seibert, J., Magnusson, J., and Jonas, T.: Assessing the benefit of snow data assimilation for runoff modeling in Alpine catchments, Hydrol. Earth Syst. Sci., 20, 3895–3905, 2016.

Griessinger, N., Schirmer, M., Helbig, N., Winstral, A., Michel, A., and Jonas, T.: Implications of observation-enhanced energy-balance snowmelt simulations for runoff modeling of Alpine catchments, Advances in Water Resources, 133, 103 410, https://doi.org/10.1016/j.advwatres.2019.103410, 2019.

Hall, D. K., Riggs, G. A., and Salomonson, V. V.: Development of methods for mapping global snow cover using moderate resolution imaging spectroradiometer data, Remote Sensing of Environment, 54, 127 – 140, https://doi.org/https://doi.org/10.1016/0034-4257(95)00137-P, 1995.

Härer, S., Bernhardt, M., and Schulz, K.: PRACTISE – Photo Rectification And ClassificaTIon SoftwarE (V.2.1), Geoscientific Model Development, 9, 307–321, https://doi.org/10.5194/gmd-9-307-2016, 2016.

Helbig, N., van Herwijnen, A., and Jonas, T.: Forecasting wet-snow avalanche probability in mountainous terrain, Cold Reg. Sci. Technol., 120, 219 – 226, https://doi.org/10.1016/j.coldregions.2015.07.001, 2015a.

Helbig, N., van Herwijnen, A., Magnusson, J., and Jonas, T.: Fractional snow-covered area parameterization over complex topography, Hydrol. Earth Syst. Sci., 19, 1339–1351, https://doi.org/10.5194/hess-19-1339-2015, 2015b.

Helbig, N., Bühler, Y., Eberhard, L., Deschamps-Berger, C., Gascoin, S., Dumont, M., Revuelto, J., Deems, J. S., and Jonas, T.: Fractional snow-covered area: Scale-independent peak of winter parameterization, The Cryosphere, 15, 615–632, https://doi.org/doi.org/10.5194/tc-15-615-2021, 2021.

Horton, S. and Jamieson, B.: Modelling hazardous surface hoar layers across western Canada with a coupled weather and snow cover model, Cold. Reg. Sci. Technol., 128, 22–31, 2016.

Huang, C., Newman, A., Clark, M. P., Wood, A. W., and Zheng, X.: Evaluation of snow data assimilation using the ensemble Kalman filter for seasonal streamflow prediction in the western United States, Hydrol. Earth Syst. Sci., 21, 635–650, https://doi.org/10.1029/JB094iB06p07491, 2017.

Höhle, J. and Höhle, M.: Accuracy assessment of digital elevation models by means of robust statistical methods, ISPRS Journal of Photogrammetry and Remote Sensing, 64, 398 – 406, https://doi.org/10.1016/j.isprsjprs.2009.02.003, 2009.

Lawrence, D., Fisher, R., Koven, C., Oleson, K., Swenson, S., and Vertenstein, M.: Technical Description of version 5.0 of the Community Land Model (CLM), https://www.cesm.ucar.edu/models/cesm2/land/CLM50_Tech_Note.pdf, [Online; accessed 31-March-2018], 2018.

López-Moreno, J. I., Revuelto, J., Alonso-Gonzáles, E., Sanmiguel-Vallelado, A., Fassnacht, S. R., Deems, J., and Morán-Tejeda, E.: Using very long-range Terrestrial Laser Scanning to Analyze the Temporal Consistency of the Snowpack Distribution in a High Mountain Environment, J. Mt. Sci., 14, 823–842, 2017.

Luce, C. H., Tarboton, D. G., and Cooley, K. R.: Sub-grid parameterization of snow distribution for an energy and mass balance snow cover model, Hydrol. Process., 13, 1921–1933, 1999.

Magand, C., Ducharne, A., Moine, N. L., and Gascoin, S.: Introducing Hysteresis in Snow Depletion Curves to Improve the Water Budget of a Land Surface Model in an Alpine Catchment, J. Hydrometeor., 15, 631–649, https://doi.org/10.1175/JHM-D-13-091.1, 2014.

Magnusson, J., Gustafsson, D., Hüsler, F., and Jonas, T.: Assimilation of point SWE data into a distributed snow cover model comparing two contrasting methods, Water Resour. Res., 50, 7816–7835, 2014.

Magnusson, J., Wever, N., Essery, R., Helbig, N., Winstral, A., and Jonas, T.: Evaluating snow models with varying process representations for hydrological applications, Water Resour. Res., 51, 2707–2723, https://doi.org/10.1002/2014WR016498, 2015.

Marty, M., Bühler, Y., and Ginzler, C.: Snow Depth Mapping, https://doi.org/10.16904/envidat.62, https://www.envidat.ch/dataset/snow-depth-mapping, 2019.

Masson, T., Dumont, M., Mura, M., Sirguey, P., Gascoin, S., Dedieu, J.-P., and Chanussot, J.: An Assessment of Existing Methodologies to Retrieve Snow Cover Fraction from MODIS Data, Remote Sensing, 10, 619, https://doi.org/10.3390/rs10040619, 2018.

Mazzotti, G., Currier, W. R., Deems, J. S., Pflug, J. M., Lundquist, J. D., and Jonas, T.: Revisiting Snow Cover Variability and Canopy Structure Within Forest Stands: Insights From Airborne Lidar Data, Water Resour. Res., 55, 6198–6216, 2019.

Mudryk, L., Santolaria-Otín, M., Krinner, G., Ménégoz, M., Derksen, C., Brutel-Vuilmet, C., Brady, M., and Essery, R.: Historical Northern Hemisphere snow cover trends and projected changes in the CMIP-6 multi-model ensemble, The Cryosphere Discussions, 2020, 1–35, https://doi.org/10.5194/tc-2019-320, 2020.

Nagler, T., Rott, H., Malcher, P., and Müller, F.: Assimilation of meteorological and remote sensing data for snowmelt runoffforecasting, Remote Sens. Environ., 112, 1408–1420, 2008.

Nitta, T., Yoshimura, K., Takata, K., O'ishi, R., Sueyoshi, T., Kanae, S., Oki, T., Abe-Ouchi, A., and Liston, G. E.: Representing Variability in Subgrid Snow Cover and Snow Depth in a Global Land Model: Offline Validation, J. Climate, 27, 3318–3330, https://doi.org/10.1175/JCLI-D-13-00310.1, 2014.

Niu, G. Y. and Yang, Z. L.: An observation-based formulation of snow cover fraction and its evaluation over large North American river basins, J. Geophys. Res., 112, https://doi.org/10.1029/2007JD008674, 2007.

Painter, T., Berisford, D., Boardman, J., Bormann, K., Deems, J., Gehrke, F., Hedrick, A., Joyce, M., Laidlaw, R., Marks, D., Mattmann, C., Mcgurk, B., Ramirez, P., Richardson, M., Skiles, S. M., Seidel, F., and Winstral, A.: The Airborne Snow Observatory: fusion of scanning lidar, imaging spectrometer, and physically-based modeling for mapping snow water equivalent and snow albedo, Remote Sens. Environ., 184, 139–152, https://doi.org/10.1016/j.rse.2016.06.018, 2016.

Painter, T. H., Rittger, K., McKenzie, C., Slaughter, P., Davis, R. E., and Dozier, J.: Retrieval of subpixel snow covered area, grain size, and albedo from MODIS, Remote Sensing of Environment, 113, 868 – 879, https://doi.org/https://doi.org/10.1016/j.rse.2009.01.001, http://www.sciencedirect.com/science/article/pii/S0034425709000029, 2009.

Parajka, J. and Blöschl, G.: Validation of MODIS snow cover images over Austria, Hydrol. Earth Syst. Sci. Discuss., 3, 1569–1601, 2006.

Portenier, C., Hüsler, F., Härer, S., and Wunderle, S.: Towards a webcam-based snow cover monitoring network: methodology and evaluation, Cryosphere, 14, 1409–1423, https://doi.org/10.5194/tc-14-1409-2020, 2020.

Revuelto, J., López-Moreno, J. I., Azorín-Molina, C., and Vicente-Serrano, S.: Topographic control of snowpack distribution in a small catchment in the central Spanish Pyrenees: intra- and inter-annual persistence, Cryosphere, 6, 1989–2006, 2014.

Riboust, P., Thirel, G., Le Moine, N., and Ribstein, P.: Revisiting a simple degree-day model for integrating satellite data: implementation of SWE-SCA hystereses, J. Hydrol. Hydromech., 67, 70–81, 2019.

Roesch, A., Wild, M., Gilgen, H., and Ohmura, A.: A new snow cover fraction parameterization for the ECHAM4 GCM, Clim. Dyn., 17, 933–946, 2001.

Salvatori, R., Plini, P., Giusto, M., Valt, M., Salzano, R., Montagnoli, M., Cagnati, A., Crepaz, G., and Sigismondi, D.: Snow cover monitoring with images from digital camera systems, Ital. J. Remote. Sens., 43, https://doi.org/10.5721/ItJRS201143211, 2011.

Schirmer, M. and Lehning, M.: Persistence in intra-annual snow depth distribution: 2. Fractal analysis of snow depth development, Water Resour. Res., 47, https://doi.org/10.1029/2010WR009429, 2011.

Schirmer, M., Wirz, V., Clifton, A., and Lehning, M.: Persistence in intra-annual snow depth distribution: 1. Measurements and topographic control, Water Resour. Res., 47, 2011.

Skaugen, T. and Melvold, K.: Modeling the snow depth variability with a high-resolution lidar data set and nonlinear terrain dependency, Water Resour. Res., 55, 9689–9704, https://doi.org/10.1029/2019WR025030, 2019.

Su, H., Yang, Z. L., Niu, G. Y., and Dickinson, R. E.: Enhancing the estimation of continental-scale snow water equivalent by assimilating MODIS snow cover with the ensemble Kalman filter, J. Geophys. Res., 113, 2008.

Swenson, S. C. and Lawrence, D. M.: A new fractional snow-covered area parameterization for the Community Land Model and its effect on the surface energy balance, Journal of Geophysical Research: Atmospheres, 117, https://doi.org/10.1029/2012JD018178, 2012.

Thirel, G., Salamon, P., Burek, P., and Kalas, M.: Assimilation of MODIS snow cover area data in a distributed hydrological model using the particle filter, Remote Sensing, 5, 5825–5850, 2013.

van Herwijnen, A. and Schweizer, J.: Seismic sensor array for monitoring an avalanche start zone: design, deployment and preliminary results, J. Glaciol., 57, 257–264, 2011.

van Herwijnen, A., Berthod, N., Simenhois, R., and Mitterer, C.: Using time-lapse photography in avalanche research, in: Proceedings of the International Snow Science Workshop, Grenoble, France, pp. 950–954, 2013.

Vionnet, V., Martin, E., Masson, V., Guyomarc'h, G., Naaim-Bouvet, F., Prokop, A., Durand, Y., and Lac, C.: Simulation of wind-induced snow transport and sublimation in alpine terrain using a fully coupled snowpack/atmosphere model, Cryosphere, 8, 395–415, 2014.

Yakir, B.: Nonparametric Tests: Kolmogorov-Smirnov and Peacock, chap. 6, pp. 103–124, John Wiley & Sons, Ltd, https://doi.org/10.1002/9781118720608.ch6, 2013.

Yang, Z. L., Dickinson, R. E., Robock, A., and Vinnikov, K. Y.: On validation of the snow sub-model of the biosphere atmosphere transfer scheme with Russian snow cover and meteorological observational data, J. Climate, 10, 353–373, 1997.

Zaitchik, B. F. and Rodell, M.: Forward-Looking Assimilation of MODIS-Derived Snow-Covered Area into a Land Surface Model, Journal of Hydrometeorology, 10, 130 – 148, https://doi.org/10.1175/2008JHM1042.1, 2009.